JOURNAL OF GEOPHYSICAL RESEARCH, VOL. 104, NO. E4, PAGES 8809–8830, APRIL 25, 1999

Preliminary results on photometric properties of materials at the Sagan Memorial Station, Mars

Jeffrey R. Johnson,[1] Randolph Kirk,[1] Laurence A. Soderblom,[1] Lisa Gaddis,[1] Robert J. Reid,[2] Daniel T. Britt,[2] Peter Smith,[2] Mark Lemmon,[2] Nicolas Thomas,[3] James F. Bell III,[4] Nathan T. Bridges,[5] Robert Anderson,[5] Ken E. Herkenhoff,[5,6] Justin Maki,[5] Scott Murchie,[7] Andreas Dummel,[8,9] Ralf Jaumann,[8] Frank Trauthan,[8] and Gabriele Arnold[8]

Abstract. Reflectance measurements of selected rocks and soils over a wide range of illumination geometries obtained by the Imager for Mars Pathfinder (IMP) camera provide constraints on interpretations of the physical and mineralogical nature of geologic materials at the landing site. The data sets consist of (1) three small "photometric spot" subframed scenes, covering phase angles from 20° to 150°; (2) two image strips composed of three subframed images each, located along the antisunrise and antisunset lines (photometric equator), covering phase angles from ~0° to 155°; and (3) full-image scenes of the rock "Yogi," covering phase angles from 48° to 100°. Phase functions extracted from calibrated data exhibit a dominantly backscattering photometric function, consistent with the results from the Viking lander cameras. However, forward scattering behavior does appear at phase angles >140°, particularly for the darker gray rock surfaces. Preliminary efforts using a Hapke scattering model are useful in comparing surface properties of different rock and soil types but are not well constrained, possibly due to the incomplete phase angle availability, uncertainties related to the photometric function of the calibration targets, and/or the competing effects of diffuse and direct lighting. Preliminary interpretations of the derived Hapke parameters suggest that (1) red rocks can be modeled as a mixture of gray rocks with a coating of bright and dark soil or dust, and (2) gray rocks have macroscopically smoother surfaces composed of microscopically homogeneous, clear materials with little internal scattering, which may imply a glass-like or varnished surface.

1. Introduction

Multispectral imaging of the Mars Pathfinder landing site (Sagan Memorial Station (SMS), Figure 1) by the Imager for Mars Pathfinder (IMP) stereo camera has provided a unique visible to near-infrared data set on local rocks and soils [*Golombek et al.*, 1997; *Smith et al.*, 1997b]. This information, in combination with elemental analyses [*Rieder et al.*, 1997], magnetic properties results [*Hviid et al.*, 1997], and morphology of surface materials [*Rover Team*, 1997; *Smith et al.*, 1997b], provides important constraints relevant to understanding more precisely the physical and mineralogical nature and distribution of soils, rock types, dust, and coatings on rocks at the SMS [cf. *McSween et al.*, this issue; J.F. Bell III et al., Mineralogic and compositional properties of martian soil and dust: Preliminary results from Mars Pathfinder, submitted to *Journal of Geophysical Research*, 1999; hereafter referred to as submitted paper]. Interpretations of reflectance spectra are influenced by the ability to discriminate spectral differences due to composition or grain size from variations in spectral response due to lighting and viewing geometry conditions. This issue was addressed specifically during Pathfinder mission operations by the design and acquisition of IMP multispectral imaging sequences to provide reflectance measurements of selected rocks and soils over a wide range of phase angles.

Photometric properties are routinely studied using radiative transfer models such as Hapke theory [e.g., *Hapke*, 1993] for objects such as the Moon [*Helfenstein and Veverka*, 1987; *Buratti et al.*, 1996; *McEwen*, 1996; *Helfenstein et al.*, 1997], Mercury [*Veverka et al.*, 1988; *Blewett et al.*, 1997], the icy satellites [*Domingue and Hapke*, 1992; *Domingue et al.*, 1997], asteroids [*Helfenstein et al.*, 1996; *Clark et al.*, 1998], and terrestrial soils and vegetation [*Liang and Townshend*, 1996; *Privette et al.*, 1995]. Photometry of Martian surface materials and atmospheric dust has been studied using Viking lander spectral imaging covering the ~400-740 nm region [*Huck et al.*, 1977; *Hapke*, 1979; *Pollack et al.*, 1979, 1995;

[1]Branch of Astrogeology, U.S. Geological Survey, Flagstaff, Arizona.
[2]Lunar and Planetary Laboratory, University of Arizona, Tucson.
[3]Max Planck Institute for Aeronomy, Katlenburg-Lindau, Germany.
[4]Center for Radiophysics and Space Research, Cornell University, Ithaca, New York.
[5]Jet Propulsion Laboratory, Pasadena, California.
[6]Now at Branch of Astrogeology, U.S. Geological Survey, Flagstaff, Arizona.
[7]Applied Physics Laboratory, Johns Hopkins University, Laurel, Maryland.
[8]Deutsche Luft-und Raunfahrt, Institute of Planetary Exploration, Berlin, Germany.
[9]Now at Eurocopter Deutschland GmbH, Muenchen, Germany.

Paper number 98JE02247.
0148-0227/99/98JE-02247$09.00

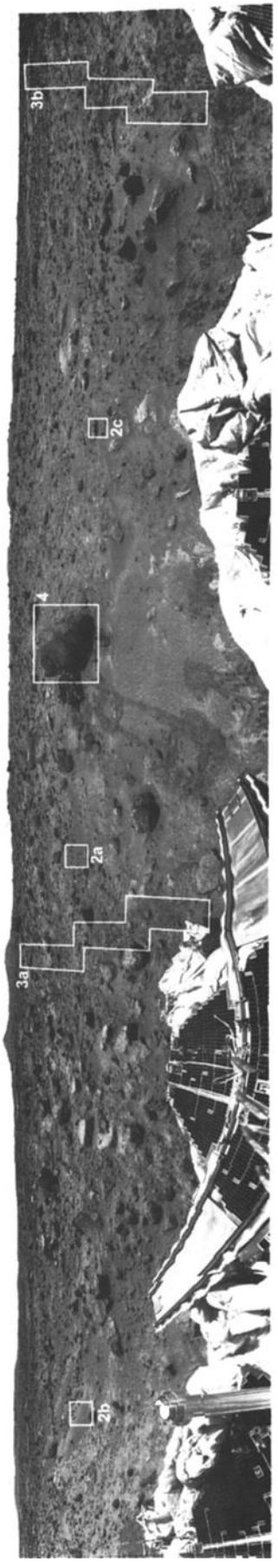

Figure 1. The Mars Pathfinder landing site (Sagan Memorial Station) imaged for the Gallery Panorama sequence obtained on sols 9-11 (monochrome version of enhanced color mosaic produced by the U.S. Geological Survey, Flagstaff). Outlined boxes show locations and figure numbers of photometric imaging sequences (Figures 2-4).

Adams et al., 1986; *Guinness et al.*, 1979, 1987, 1996, 1997a,b; *Arvidson et al.*, 1989a,b], telescopic imaging and spectroscopy [*Binder and Jones*, 1972; *deGrenier and Pinet*, 1995; *Bell et al.*, 1999], Viking orbiter and Mariner 9 imaging [*Thorpe*, 1977; *Young and Collins*, 1971], including analyses of Phobos [*Simonelli et al.*, 1998] and Deimos [*Thomas et al.*, 1996], Viking Infrared Thermal Mapper (IRTM) observations [*Clancy and Lee*, 1991; *Clancy et al.*, 1995], and Phobos II Infrared Spectrometer for Mars (ISM) data [e.g., *Erard*, 1998]. A major goal of such efforts is photometric correction of spectral data to common illumination geometries, which allows equivalent comparison of data obtained at different times of day [e.g., *Kirkland et al.*, 1997]. Additionally, photometric functions can be modeled to constrain parameters used to interpret surface properties (e.g., porosity, grain size distribution). Here we present and describe the available IMP multispectral data sets reduced using Version 1 of the IMP calibration algorithm [*Reid et al.*, this issue]. We examine phase curves extracted from the IMP photometric imaging sequences and use a Hapke scattering model [*Domingue et al.*, 1997] to model phase curves that have sufficient phase angle coverage. Preliminary analyses of the photometric properties of various surface materials are then compared to previous work on Mars surface photometry.

2. Data Sets and Calibration

The IMP stereo camera system was composed of two eyes, each of which illuminated half of a single 512x256-pixel CCD detector [*Smith et al.*, 1997*a*] with a field-of-view of 14°. A total of 24 filters were available (12 for each eye), of which 15 were designed for imaging geologic materials from 440 to 1000 nm. Multispectral images of specific targets using a selection of these filters in "left" and/or "right" eyes were obtained by executing a series of programmed IMP camera commands, which are referred to as "imaging sequences." Five such imaging sequences designed and written by the authors to provide reflectance measurements of rocks and soils over a wide range of phase angles were executed by the IMP camera. Three of the resulting data sets consist of small, "photometric spot" subframed (64x64 pixel), losslessly compressed scenes located approximately north (near the rock nicknamed "Shaggy"), south (near the "Mermaid Dune"), and west of the lander ("Photometry Flats") (Figures 1 and 2). These images were obtained in six filters at six times of day (Local True Solar Time, LTST) covering phase angles from 20° to 150° (Tables 1a-1c). All areas were chosen to contain materials sunlit at all times of day. Photometry Flats was chosen as an example of "dark soil" [cf. *Smith et al.*, 1997b], the Shaggy area as examples of rocks and soil, and the Mermaid area as an example of different surface materials (including areas driven on and excavated by the rover wheels). We note that slight IMP camera pointing uncertainties [*Smith et al.*, 1997a] resulted in minor pointing repeatability differences within a given imaging sequence; this is particularly apparent in the photometric spot sequences (Figure 2).

Another sequence obtained two image strips composed of three subframed (96x248 pixel), losslessly compressed images each, located in the principal plane along the antisunrise (Figure 3a) and antisunset (Figure 3b) lines

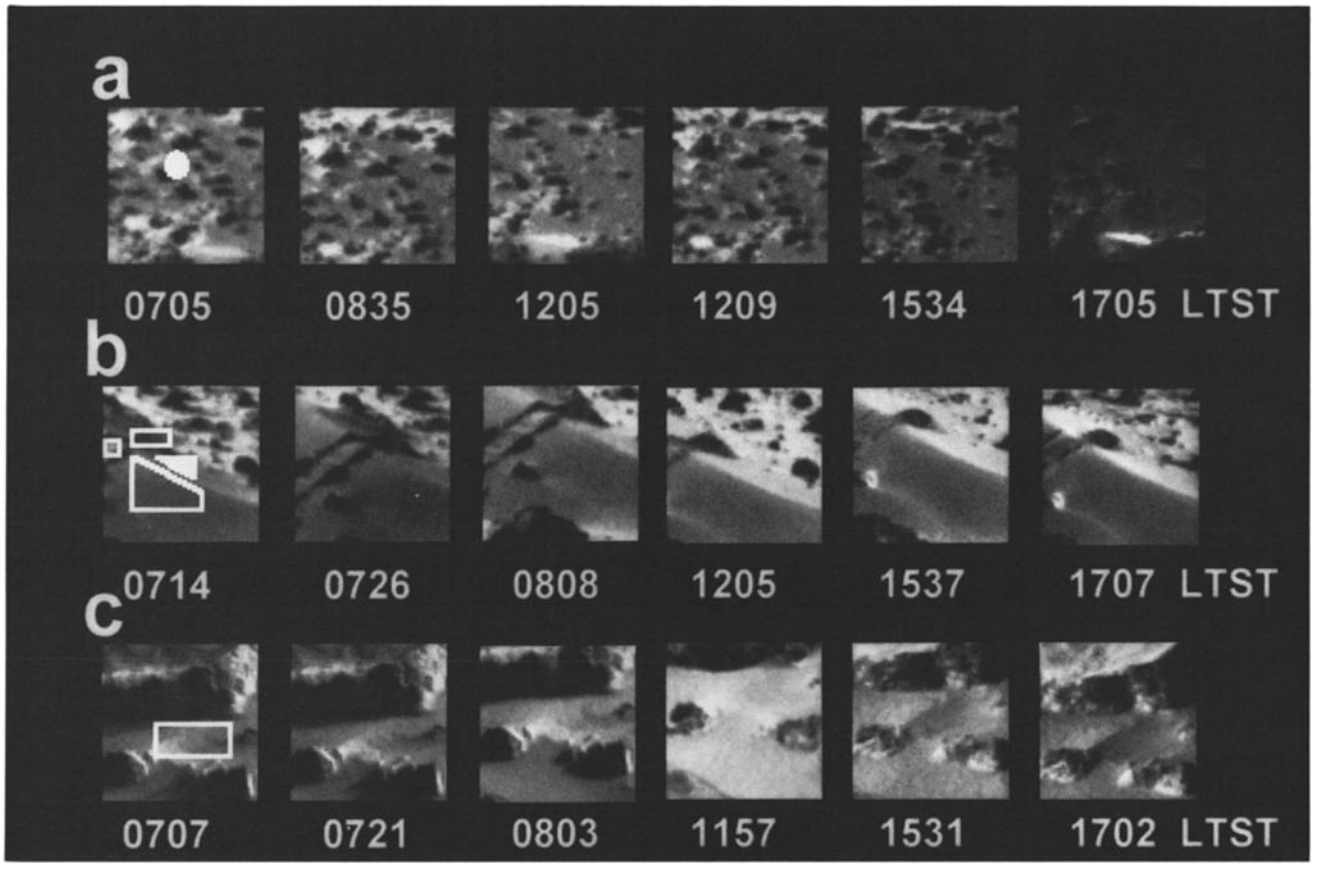

Figure 2. Images (752 nm) of photometric spot sequences of (a) Photometry Flats area, showing location of soil spectrum in leftmost image (solid oval); (b) Mermaid dune area, showing approximate locations from which spectra were obtained for the flat track (open square), bright soil (solid polygon), dark soil (open polygon), and disturbed pile (open rectangle) samples; and (c) Shaggy rock area, showing location of soil spectrum (open rectangle). Acquisition times (LTST) shown below each image. See Figure 1 for locations and Tables 1a-1c. Note that slight IMP camera pointing uncertainties [*Smith et al*, 1997a] resulted in minor pointing repeatability differences within a given imaging sequence.

("photometric equator") extending from near the lander ("near-field") to near the horizon ("far-field"). This data set was obtained in three filters at four times of day covering phase angles from ~0° to 155° (Tables 1d,1e).

The fifth photometric imaging sequence was composed of full-image (256 x 248 pixel) scenes with 6:1 lossy image compression of the large rock nicknamed "Yogi" (Figure 4) obtained in four filters at four times of day over three different sols covering phase angles 47° to 111° (Table 1f). The effects of image compression are principally geometric (reduction in effective spatial resolution). Lossless compression does not affect the radiometric precision of the data, and the low-level lossy compression of the Yogi data decreases the signal-to-noise by < 2% [*Reid et al.*, this issue].

Images were radiometrically calibrated to R^* using onboard calibration targets imaged at or near the same time of day and Version 1 of the IMP calibration algorithm, as documented by *Reid et al.* [this issue]. Briefly, R^* is the total radiance in each pixel of the image relative to the total radiance of the calibration targets, scaled by their "known" laboratory reflectances. In this sense, R^* is approximately equivalent to the reflectance factor (coefficient) of *Hapke* [1993, p. 262], defined as the ratio of the reflectance of a given surface to that of a Lambertian surface under the same conditions of illumination and measurement. The non-Lambertian nature of the calibration targets has not been accounted for in the current version of the IMP calibration algorithm [*Reid et al.*, this issue]. Neither has a detailed atmospheric model been used to correct for the effects of reddened diffuse skylight on the image scene [*Reid et al.*, this issue; *Thomas et al.*, this issue]. This effect is most pronounced for large, multifaceted rocks (such as Yogi), which show increased red reflectance when a greater proportion of reddened diffuse skylight illuminates a given facet than direct sunlight [cf. *Thomas et al.*, this issue; *Tomasko et al.*, this issue]. However, the first-order effects of such atmospheric contributions are subtracted and minimized by obtaining calibration target and scene images close in time under similar illumination geometries, particularly for relatively flat surfaces. Typical uncertainties on the absolute reflectance derived in Version 1 of the calibration are ~10% [*Reid et al.*, this issue].

Calibration target images were obtained as part of the photometric spot imaging sequences, and separate calibration

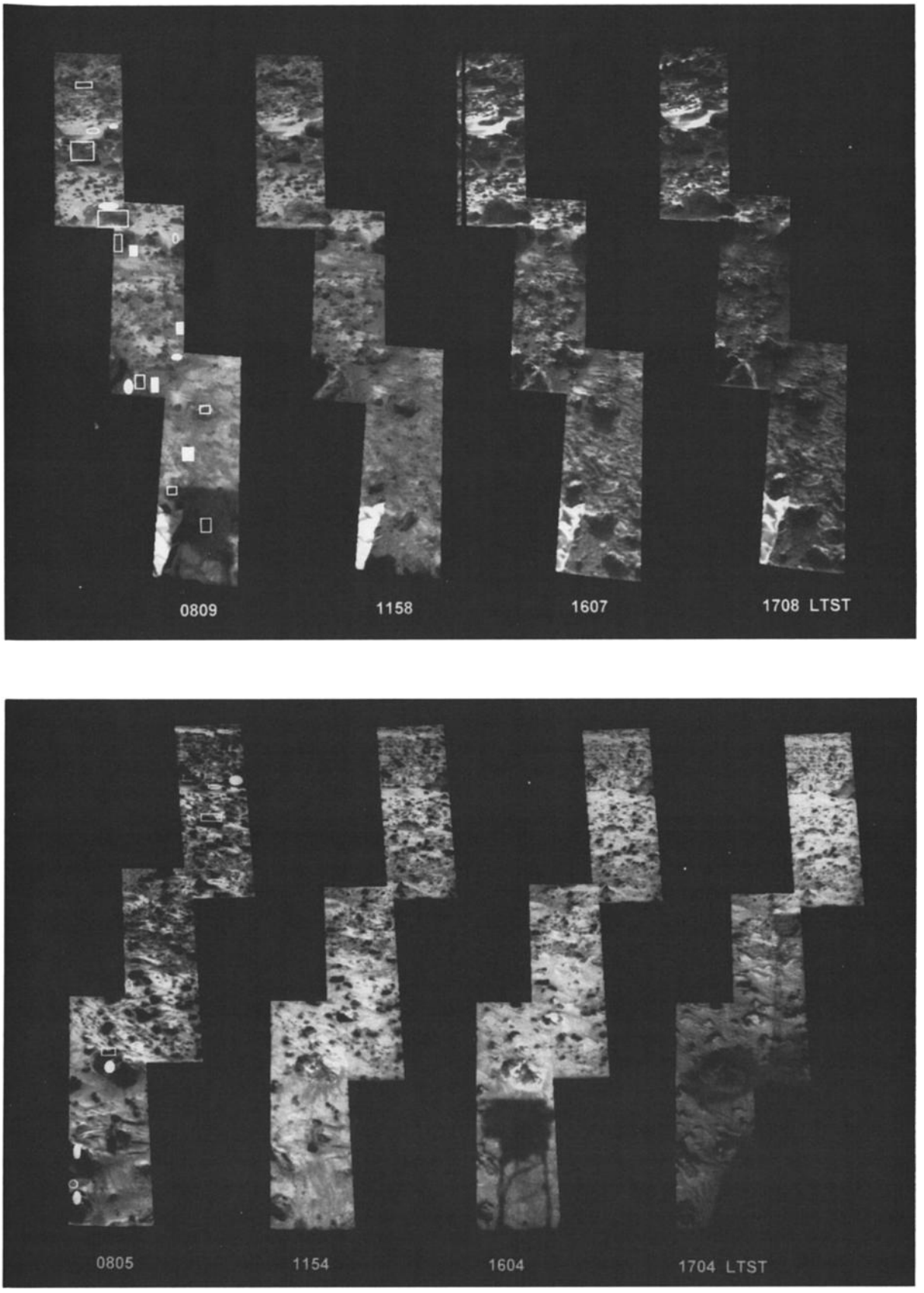

Figure 3. Image mosaics (752 nm) of photometric equator sequences of (a) antisunrise and (b) antisunset regions. First column of images shows approximate locations from which cumulative spectra were obtained for gray rock (open rectangles), red rock (solid ovals), bright soil (open ovals), and dark soil units (solid rectangles) (Figure 7). Acquisition times (LTST) shown below each image. Details of observations given in Tables 1d, 1e. Note shadow of IMP camera head in 0809, 1604, and 1704 LTST observations.

Table 1a. Photometry Flats Photometric Sequence Images

SCLK Time--Image ID (IMP-EDR (REGULAR))	Sol	LTST	Filter	Wavelength, nm	Incidence Angle, deg	Emission Angle, deg	Phase Angle, deg
1248517042--0190020015	21	0704:01	R 0	443	71.4	77.6	19.8
1248517059--0190020017	21	0704:18	R 11	968	71.4	77.6	19.8
1248517076--0190020019	21	0704:34	R 9	531	71.3	77.6	19.8
1248517094--0190020021	21	0704:52	R 6	752	71.2	77.6	19.8
1248517109--0190020023	21	0705:06	R 5	671	71.2	77.6	19.8
1248517125--0190020024	21	0705:22	L 7	858	71.1	77.6	19.3
1248522584--0190020015	21	0833:55	R 0	443	50.2	77.6	29.5
1248522600--0190020017	21	0834:11	R 11	968	50.2	77.6	29.5
1248522617--0190020019	21	0834:27	R 9	531	50.1	77.6	29.6
1248522635--0190020021	21	0834:45	R 6	752	50.0	77.6	29.6
1248522650--0190020023	21	0835:00	R 5	671	50.0	77.6	29.7
1248522666--0190020024	21	0835:15	L 7	858	49.9	77.6	29.6
1248535551--0190020015	21	1204:17	R 0	443	8.2	77.6	76.8
1248535569--0190020017	21	1204:34	R 11	968	8.2	77.6	76.8
1248535588--0190020019	21	1204:53	R 9	531	8.2	77.6	76.9
1248535608--0190020021	21	1205:12	R 6	752	8.2	77.6	77.0
1248535624--0190020023	21	1205:28	R 5	671	8.2	77.6	77.1
1248535643--0190020024	21	1205:46	L 7	858	8.2	77.6	77.2
1248535827--0195020029	21	1208:45	R 0	443	8.4	77.6	77.8
1248535846--0195020031	21	1209:04	R 11	968	8.4	77.6	77.9
1248535864--0195020033	21	1209:21	R 9	531	8.4	77.6	78.0
1248535884--0195020035	21	1209:41	R 6	752	8.4	77.6	78.1
1248535901--0195020037	21	1209:57	R 5	671	8.5	77.6	78.1
1248535919--0195020038	21	1210:15	L 7	858	8.5	77.6	78.3
1248548424--0195020029	21	1533:07	R 0	443	51.9	77.6	127.6
1248548441--0195020031	21	1533:23	R 11	968	52.0	77.6	127.7
1248548457--0195020033	21	1533:39	R 9	531	52.0	77.6	127.7
1248548475--0195020035	21	1533:56	R 6	752	52.1	77.6	127.8
1248548490--0195020037	21	1534:11	R 5	671	52.2	77.6	127.9
1248548506--0195020038	21	1534:27	L 7	858	52.2	77.6	128.1
1248554018--0195020029	21	1703:52	R 0	443	73.3	77.6	149.9
1248554037--0195020031	21	1704:10	R 11	968	73.4	77.6	149.9
1248554055--0195020033	21	1704:28	R 9	531	73.5	77.6	150.0
1248554073--0195020035	21	1704:45	R 6	752	73.5	77.6	150.1
1248554088--0195020037	21	1705:00	R 5	671	73.6	77.6	150.1
1248554105--0195020038	21	1705:16	L 7	858	73.7	77.6	150.4

LTST has been calculated using the spacecraft clock (SCLK) time and Solar System Calculator. Incident, emission, and phase angles have been calculated for the center of each image.

target imaging sequences were obtained close in time to the Yogi image sequences. However, calibration target imaging sequences intended to accompany the photometric equator sequences were not obtained due to spacecraft downlink difficulties. Therefore calibration target images were used from the Photometry Flats sequences obtained 6 sols earlier because these provided images obtained in the same filters and at the same times of day. (Differences in atmospheric opacity are most significant for the ~0830 LTST 450 nm measurements between sol 21 ($\tau \sim 0.62$) and sol 27 ($\tau \sim 0.51$), which might affect derived R^* values for the 443 nm band [*Reid et al,*. this issue; *Smith and Lemmon,* this issue]).

Once calibrated, multispectral images for each LTST observation were spatially registered using subpixel linear transformations, and image cubes were constructed for both left- and right-eye images (only the Photometry Flats sequence included a left-eye filter). For the photometric equator data set shown in Figure 3, the three scenes obtained at a given LTST were mosaicked by first projecting each three-band image cube to a geometrically controlled panoramic map projection using ISIS software [*Gaddis et al.,* 1997, this issue; *Eliason,* 1997; *Kirk et al.,* this issue]. Then a simultaneous least squares solution algorithm was applied to allow subpixel spatial registration and mosaicking of the three image cubes. Spectra were extracted for regions of interest from each LTST image cube mosaic. Phase angles were calculated for the center of each image. For the small photometric spot images (Figure 2), this value was assigned to all materials in the scene because the phase angle varied by only ±1.7° within the scene. However, for soils and rocks sampled away from the centers of the larger photometric equator images (Figure 3), phase angles were calculated by extrapolation from the center phase angle value. We note that for the Yogi sequence, only the south-facing portion of the rock face is illuminated at all daylight hours (Figure 4), and surface facet geometric information is necessary for accurate

Table 1b. Mermaid Dune Area Photometric Sequence Images

SCLK Time--Image ID (IMP-EDR (REGULAR))	Sol	LTST	Filter	Wavelength, nm	Incidence Angle, deg	Emission Angle, deg	Phase Angle, deg
1250044632--0194010063	38	1204:27	R 0	443	11.8	77.2	87.7
1250044649--0194010065	38	1204:44	R 11	967	11.8	77.2	87.7
1250044664--0194010067	38	1204:58	R 10	480	11.8	77.2	87.6
1250044680--0194010069	38	1205:14	R 9	531	11.8	77.2	87.6
1250044698--0194010071	38	1205:32	R 6	752	11.9	77.2	87.6
1250044713--0194010073	38	1205:46	R 5	671	11.9	77.2	87.6
1250057679--0195030063	38	1536:05	R 0	443	53.7	77.2	68.6
1250057696--0195030065	38	1536:22	R 11	967	53.8	77.2	68.6
1250057711--0195030067	38	1536:37	R 10	480	53.8	77.2	68.6
1250057726--0195030069	38	1536:51	R 9	531	53.9	77.2	68.6
1250057744--0195030071	38	1537:09	R 6	752	53.9	77.2	68.6
1250057758--0195030073	38	1537:22	R 5	671	54.0	77.2	68.5
1250063269--0195030063	38	1706:46	R 0	443	75.1	77.2	63.0
1250063288--0195030065	38	1707:05	R 11	967	75.2	77.2	63.0
1250063303--0195030067	38	1707:19	R 10	480	75.2	77.2	63.0
1250063319--0195030069	38	1707:35	R 9	531	75.3	77.2	62.9
1250063337--0195030071	38	1707:53	R 6	752	75.4	77.2	62.9
1250063352--0195030073	38	1708:07	R 5	671	75.4	77.2	62.9
1250115475--0194010063	39	0713:36	R 0	443	70.3	77.2	105.0
1250115494--0194010065	39	0713:55	R 11	967	70.3	77.2	105.0
1250115510--0194010067	39	0714:11	R 10	480	70.2	77.2	105.0
1250115526--0194010069	39	0714:26	R 9	531	70.1	77.2	105.0
1250115544--0194010071	39	0714:44	R 6	752	70.1	77.2	105.0
1250115558--0194010073	39	0714:57	R 5	671	70.0	77.2	105.0
1250116192--0190030063	39	0725:14	R 0	443	67.6	77.2	104.9
1250116210--0190030065	39	0725:32	R 11	967	67.5	77.2	104.9
1250116226--0190030067	39	0725:47	R 10	480	67.5	77.2	104.9
1250116241--0190030069	39	0726:02	R 9	531	67.4	77.2	104.9
1250116259--0190030071	39	0726:20	R 6	752	67.3	77.2	104.9
1250116274--0190030073	39	0726:34	R 5	671	67.3	77.2	104.9
1250118782--0190030063	39	0807:15	R 0	443	57.7	77.2	103.9
1250118799--0190030065	39	0807:32	R 11	967	57.6	77.2	103.9
1250118814--0190030067	39	0807:46	R 10	480	57.5	77.2	103.9
1250118829--0190030069	39	0808:01	R 9	531	57.5	77.2	103.9
1250118847--0190030071	39	0808:19	R 6	752	57.4	77.2	103.9
1250118862--0190030073	39	0808:33	R 5	671	57.4	77.2	103.9

We note that additional but incomplete photometric imaging sequences of this area were obtained on sol 55 (~1700 LTST) and sol 56 (~ 0720 and ~ 0800 LTST) but are not used in this study.

photometric and photoclinometric analysis. Thus we defer modeling the photometric parameters of Yogi rock until future stereo models can provide local facet orientations [cf. *Kirk et al.*, this issue; *Gaddis et al.*, this issue], and more detailed atmospheric scattering corrections are available [cf. *Thomas et al.*, this issue]. For now, the relevant image data and viewing geometries for Yogi (assuming a flat surface) are presented in Table 1f.

3. Phase Curves

3.1. Photometric Spots

Phase curves for the photometric spot sequences are shown in Figures 5 and 6. The soil in Photometry Flats (Figure 5a) exhibits strong backscattering at phase angles <40° and a minor forward scattering lobe at 443 nm and 531 nm for angles >140°, with little variation among the other filters.

Table 1c. Shaggy Rock Area Photometric Sequence Images

SCLK Time--Image ID (IMP-EDR (REGULAR))	Sol	LTST	Filter	Wavelength, nm	Incidence Angle, deg	Emission Angle, deg	Phase Angle, deg
1250044156--0194010003	38	1156:44	R 0	443	11.8	72.9	61.9
1250044172--0194010005	38	1157:00	R 11	967	11.8	72.9	61.9
1250044188--0194010007	38	1157:15	R 10	480	11.8	72.9	61.9
1250044203--0194010009	38	1157:30	R 9	531	11.8	72.9	61.9
1250044222--0194010011	38	1157:48	R 6	752	11.8	72.9	61.9
1250044237--0194010013	38	1158:03	R 5	671	11.8	72.9	61.8
1250057346--0195030003	38	1530:41	R 0	443	52.4	72.9	62.2
1250057363--0195030005	38	1530:58	R 11	967	52.5	72.9	62.2
1250057377--0195030007	38	1531:11	R 10	480	52.5	72.9	62.3
1250057392--0195030009	38	1531:26	R 9	531	52.6	72.9	62.3
1250057410--0195030011	38	1531:44	R 6	752	52.7	72.9	62.3
1250057425--0195030013	38	1531:58	R 5	671	52.7	72.9	62.3
1250062927--0195030003	38	1701:13	R 0	443	73.8	72.9	71.9
1250062945--0195030005	38	1701:31	R 11	967	73.9	72.9	71.9
1250062960--0195030007	38	1701:46	R 10	480	73.9	72.9	71.9
1250062976--0195030009	38	1702:01	R 9	531	74.0	72.9	72.0
1250062994--0195030011	38	1702:19	R 6	752	74.1	72.9	72.0
1250063008--0195030013	38	1702:32	R 5	671	74.1	72.9	72.0
1250115017--0194010003	39	0706:11	R 0	443	72.1	72.9	101.2
1250115035--0194010005	39	0706:28	R 11	967	72.0	72.9	101.1
1250115050--0194010007	39	0706:43	R 10	480	72.0	72.9	101.1
1250115065--0194010009	39	0706:57	R 9	531	71.9	72.9	101.1
1250115084--0194010011	39	0707:16	R 6	752	71.8	72.9	101.0
1250115098--0194010013	39	0707:29	R 5	671	71.8	72.9	101.0
1250115910--0190030003	39	0720:40	R 0	443	68.7	72.9	98.9
1250115927--0190030005	39	0720:56	R 11	967	68.6	72.9	98.8
1250115942--0190030007	39	0721:11	R 10	480	68.5	72.9	98.8
1250115958--0190030009	39	0721:27	R 9	531	68.5	72.9	98.7
1250115976--0190030011	39	0721:44	R 6	752	68.4	72.9	98.7
1250115990--0190030013	39	0721:58	R 5	671	68.4	72.9	98.7
1250118503--0190030003	39	0802:44	R 0	443	58.7	72.9	92.2
1250118520--0190030005	39	0803:00	R 11	967	58.7	72.9	92.1
1250118535--0190030007	39	0803:15	R 10	480	58.6	72.9	92.1
1250118550--0190030009	39	0803:29	R 9	531	58.6	72.9	92.0
1250118568--0190030011	39	0803:47	R 6	752	58.5	72.9	92.0
1250118582--0190030013	39	0804:01	R 5	671	58.4	72.9	92.0

We note that additional but incomplete photometric imaging sequences of this area were obtained on sol 55 (~1700 LTST) and sol 56 (~ 0720 and ~ 0800 LTST) but are not used in this study.

The Shaggy area soil phase curve (Figure 5b) shows a peculiar, large peak in R^* at 72° phase that may be due to a side lobe of a specular scattering component (Table 1c). The Mermaid area afforded the selection of four types of surfaces from which to obtain spectral phase curves (Figure 6). This area was visited by the Sojourner rover before these images were acquired, providing examples of soil compressed by the rover track ("flat track" material in Figure 6) and soil excavated during soil mechanics experiments ("disturbed pile"), in addition to the "dark" and "bright" soils that comprise the Mermaid dune. The phase curves exhibit a minor increase in R^* past 100° for the flat track material, suggesting a forward scattering component. There is an increase in R^* from 68° to 63° phase, particularly for the bright soil. This is too large a phase angle to represent the onset of an opposition effect and may also indicate the side lobe of a specular scattering reflectance peak (Table 1b). Although neither the Shaggy nor Mermaid images was

Table 1d. Photometric Equator, Antisunrise Photometric Sequence Images

SCLK Time--Image ID (IMP-EDR (REGULAR))	Sol	LTST	Filter	Wavelength, nm	Incidence Angle, deg	Emission Angle, deg	Phase Angle, deg
				Far Field			
1249053560--0290010043	27	0807:41	R 0	443	56.8	83.0	27.5
1249053585--0290010045	27	0808:05	R 6	752	56.7	83.0	27.6
1249053606--0290010047	27	0808:25	R 11	967	56.6	83.0	27.7
1249067668--0295010043	27	1156:33	R 0	443	9.4	83.0	83.6
1249067693--0295010045	27	1156:57	R 6	752	9.4	83.0	83.7
1249067715--0295010047	27	1157:18	R 11	967	9.4	83.0	83.8
1249083067--0295010043	27	1606:22	R 0	443	60.1	83.0	142.2
1249083093--0295010045	27	1606:47	R 6	752	60.2	83.0	142.3
1249083114--0295010047	27	1607:08	R 11	967	60.3	83.0	142.3
1249086782--0295010043	27	1706:38	R 0	443	74.3	83.0	153.8
1249086811--0295010045	27	1707:06	R 6	752	74.5	83.0	153.8
1249086832--0295010047	27	1707:27	R 11	967	74.5	83.0	153.9
				Mid Field			
1249053625--0290010053	27	0808:44	R 0	443	56.5	70.6	14.7
1249053649--0290010055	27	0809:07	R 6	752	56.4	70.6	14.8
1249053671--0290010057	27	0809:29	R 11	967	56.4	70.6	14.9
1249067735--0295010053	27	1157:38	R 0	443	9.4	70.6	71.0
1249067760--0295010055	27	1158:02	R 6	752	9.4	70.6	71.1
1249067782--0295010057	27	1158:23	R 11	967	9.4	70.6	71.2
1249083133--0295010053	27	1607:26	R 0	443	60.4	70.6	130.8
1249083160--0295010055	27	1607:53	R 6	752	60.5	70.6	130.9
1249083181--0295010057	27	1608:13	R 11	967	60.6	70.6	131.0
1249086852--0295010053	27	1707:46	R 0	443	74.6	70.6	144.1
1249086883--0295010055	27	1708:16	R 6	752	74.7	70.6	144.2
1249086905--0295010057	27	1708:38	R 11	967	74.8	70.6	144.3
				Near Field			
1249053689--0290010063	27	0809:46	R 0	443	56.3	60.5	4.2
1249053714--0290010065	27	0810:10	R 6	752	56.2	60.5	4.3
1249053735--0290010067	27	0810:31	R 11	967	56.1	60.5	4.4
1249067801--0295010063	27	1158:42	R 0	443	9.4	60.5	60.5
1249067827--0295010065	27	1159:07	R 6	752	9.4	60.5	60.6
1249067849--0295010067	27	1159:29	R 11	967	9.4	60.5	60.7
1249083199--0295010063	27	1608:31	R 0	443	60.6	60.5	121.1
1249083227--0295010065	27	1608:58	R 6	752	60.7	60.5	121.2
1249083248--0295010067	27	1609:18	R 11	967	60.8	60.5	121.3
1249086925--0295010063	27	1708:57	R 0	443	74.9	60.5	135.1
1249086958--0295010065	27	1709:29	R 6	752	75.0	60.5	135.3
1249086979--0295010067	27	1709:50	R 11	967	75.1	60.5	135.3

obtained in the principal plane (where specular scattering is most likely to be observed), the incidence and emission angles are nearly equal for the two measurements with anomalously high R^* values. Laboratory studies of the calibration targets and Mars analog materials [*Reid et al.*, this issue; *Arnold et al.*, 1998] have shown that significant side lobes of the specular scattering component can be observed up to ±60° from the principal plane. We suggest that this effect may be responsible for the high R^* values, unless they are caused by residual calibration uncertainties (e.g., due to the non-Lambertian nature of the calibration target surfaces).

3.2. Photometric Equator

To increase phase angle sampling and to constrain photometric differences among different surface materials, four units were defined in the photometric equator data (bright soil, dark soil, gray rock, and red rock) on the basis of ongoing multispectral classification work of landing site materials [*McSween et al.*, this issue; *J.F. Bell III et al.*, submitted paper, 1999]. Spectra were extracted and combined for each unit (following the methods used on Viking lander multispectral images by *Guinness et al.* [1997b]). Bright soil materials appear brighter and redder

Table 1e. Photometric Equator, Antisunset Photometric Sequence Images

SCLK Time--Image ID (IMP-EDR (REGULAR))	Sol	LTST	Filter	Wavelength, nm	Incidence Angle, deg	Emission Angle, deg	Phase Angle, deg
				Far Field			
1249053327--0290010013	27	0803:54	R 0	443	57.7	83.3	140.3
1249053353--0290010015	27	0804:19	R 6	752	57.6	83.3	140.2
1249053374--0290010017	27	0804:40	R 11	967	57.5	83.3	140.1
1249067428--0295010013	27	1152:39	R 0	443	9.5	83.3	86.4
1249067454--0295010015	27	1153:04	R 6	752	9.5	83.3	86.3
1249067476--0295010017	27	1153:26	R 11	967	9.5	83.3	86.2
1249082838--0295010013	27	1602:39	R 0	443	59.2	83.3	25.1
1249082863--0295010015	27	1603:03	R 6	752	59.3	83.3	25.0
1249082884--0295010017	27	1603:24	R 11	967	59.4	83.3	24.9
1249086546--0295010013	27	1702:48	R 0	443	73.4	83.3	10.3
1249086572--0295010015	27	1703:14	R 6	752	73.5	83.3	10.2
1249086594--0295010017	27	1703:35	R 11	967	73.6	83.3	10.1
				Mid Field			
1249053393--0290010023	27	0804:58	R 0	443	57.4	70.3	127.7
1249053419--0290010025	27	0805:23	R 6	752	57.3	70.3	127.6
1249053441--0290010027	27	0805:45	R 11	967	57.2	70.3	127.5
1249067496--0295010023	27	1153:45	R 0	443	9.5	70.3	72.7
1249067522--0295010025	27	1154:10	R 6	752	9.5	70.3	72.6
1249067544--0295010027	27	1154:32	R 11	967	9.5	70.3	72.5
1249082903--0295010023	27	1603:42	R 0	443	59.5	70.3	11.3
1249082928--0295010025	27	1604:07	R 6	752	59.6	70.3	11.2
1249082950--0295010027	27	1604:28	R 11	967	59.7	70.3	11.1
1249086613--0295010023	27	1703:54	R 0	443	73.7	70.3	3.6
1249086639--0295010025	27	1704:19	R 6	752	73.8	70.3	3.7
1249086661--0295010027	27	1704:40	R 11	967	73.9	70.3	3.8
				Near Field			
1249053459--0290010033	27	0806:02	R 0	443	57.2	60.7	117.9
1249053485--0290010035	27	0806:28	R 6	752	57.1	60.7	117.8
1249053506--0290010037	27	0806:48	R 11	967	57.0	60.7	117.7
1249067562--0295010033	27	1154:49	R 0	443	9.4	60.7	62.3
1249067588--0295010035	27	1155:15	R 6	752	9.4	60.7	62.2
1249067610--0295010037	27	1155:36	R 11	967	9.4	60.7	62.2
1249082968--0295010033	27	1604:46	R 0	443	59.7	60.7	1.2
1249082992--0295010035	27	1605:09	R 6	752	59.8	60.7	1.2
1249083014--0295010037	27	1605:30	R 11	967	59.9	60.7	1.1
1249086679--0295010033	27	1704:58	R 0	443	73.9	60.7	14.1
1249086707--0295010035	27	1705:25	R 6	752	74.1	60.7	14.3
1249086728--0295010037	27	1705:45	R 11	967	74.1	60.7	14.3

than dark soil materials, whereas gray rocks have higher 443 nm R^* and lower 752 nm and 967 nm R^* than red rocks, which are interpreted to be dust-covered [*McSween et al.*, this issue]. Approximate locations from which spectra were extracted for each unit (when not shadowed) are shown on Figure 3. The phase points for the soil materials (Figure 7a) and rocks (Figure 7b) have been fit with a cubic polynomial to provide a qualitative measure of the trends in the phase curves. Note that the gray and dark soil surfaces lack high phase angle measurements due to shadowing, while the more horizontal bright soil and red rock surfaces have greater phase angle coverage. The phase curves suggest a dominantly backscattering function, although a forward scattering component is also observed, especially for the gray rock materials.

4. Photometric Analysis

The Hapke model used by Domingue et al. [*Domingue and Hapke*, 1992; *Domingue et al.*, 1997; *Hapke*, 1984, 1986] has

Table 1f. Yogi Rock Photometric Sequence Images

SCLK Time--Image ID (IMP-EDR (REGULAR))	Sol	LTST	Filter	Wavelength, nm	Incidence Angle, deg	Emission Angle, deg	Phase Angle, deg
1251564685--0265030005	55	1500:55	R 0	443	46.9	80.0	93.9
1251564708--0265030007	55	1501:17	R 5	671	47.0	80.0	94.0
1251564735--0265030009	55	1501:43	R 9	531	47.1	80.0	94.1
1251564761--0265030011	55	1502:09	R 11	967	47.2	80.0	94.1
1251571032--0265030005	55	1643:52	R 0	443	70.9	80.0	110.4
1251571060--0265030007	55	1644:19	R 5	671	71.0	80.0	110.5
1251571088--0265030009	55	1644:47	R 9	531	71.2	80.0	110.6
1251571119--0265030011	55	1645:17	R 11	967	71.3	80.0	110.6
1251626349--0265030005	56	0741:18	R 0	443	65.1	80.0	54.7
1251626369--0265030007	56	0741:37	R 5	671	65.0	80.0	54.6
1251626390--0265030009	56	0741:58	R 9	531	64.9	80.0	54.6
1251626417--0265030011	56	0742:24	R 11	967	64.8	80.0	54.6
1253318281--0265030005	75	0904:48	R 0	443	47.7	80.0	47.8
1253318303--0265030007	75	0905:09	R 5	671	47.6	80.0	47.9
1253318320--0265030009	75	0905:26	R 9	531	47.5	80.0	47.9
1253318334--0265030011	75	0905:39	R 11	967	47.5	80.0	47.9

been slightly modified to permit use of the radiance coefficient R^* instead of radiance factor (see above [*Hapke*, 1993]). This model was used (where sufficient phase angle coverage exists) to model the scattering properties of the phase curves presented above. This radiative transfer-based model uses a grid search algorithm to minimize the least squares residual between the model and data. The search uses the parameters w (single scattering albedo), θ–bar (macroscopic roughness), b and c (single particle scattering parameters used in a double Henyey-Greenstein function), b0 (opposition effect amplitude), and h (opposition effect width), and ranks the 10 best fits to the data as determined from the residuals.

All parameters were allowed to vary without constraint except for b0, which was not allowed to be greater than 1.0 in accordance with Hapke theory [e.g., *Hapke*, 1986, 1993; *Helfenstein et al.*, 1997]. Other workers allow b0 to exceed 1.0 [e.g., *Guinness et al.*, 1997a,b; *Helfenstein et al.*, 1996], which may be permissible for cases in which the coherent backscatter effect (COBE) is important. However, COBE is a multiple-scattering phenomenon that mainly occurs at phase angles <3°. Conversely, Hapke modeling of the opposition effect assumes single scattering of light, and the data used here (Figure 7) include mainly phase angles >3°, such that the shadow-hiding effect dominates the COBE [e.g., *Helfenstein et al.*, 1997; *Hapke et al.*, 1998]. Further, COBE is particularly dominant for very bright materials (e.g., $w > 0.95$ [cf. *Nelson et al.*, 1998]), which do not occur in abundance on the Martian surface. It is thus a reasonable constraint to keep $b0 < 1.0$ for the data sets studied here.

An additional constraint to the model is that the parameters θ–bar and h are wavelength-independent [e.g., *Domingue et al.*, 1997]. However, variations with wavelength were observed for these parameters in preliminary model runs.

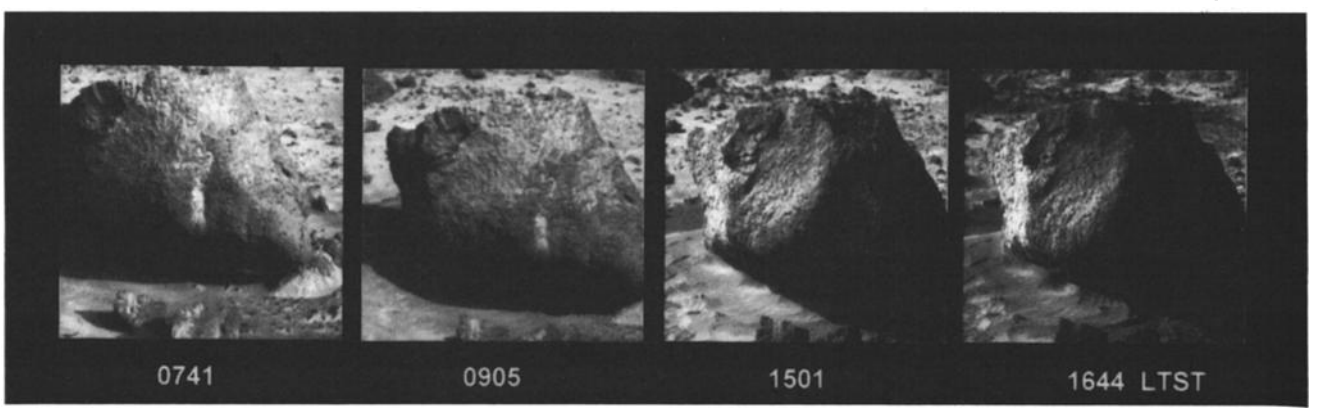

Figure 4. Images (671 nm) of Yogi rock photometric sequence. Details of observations given in Table 1f.

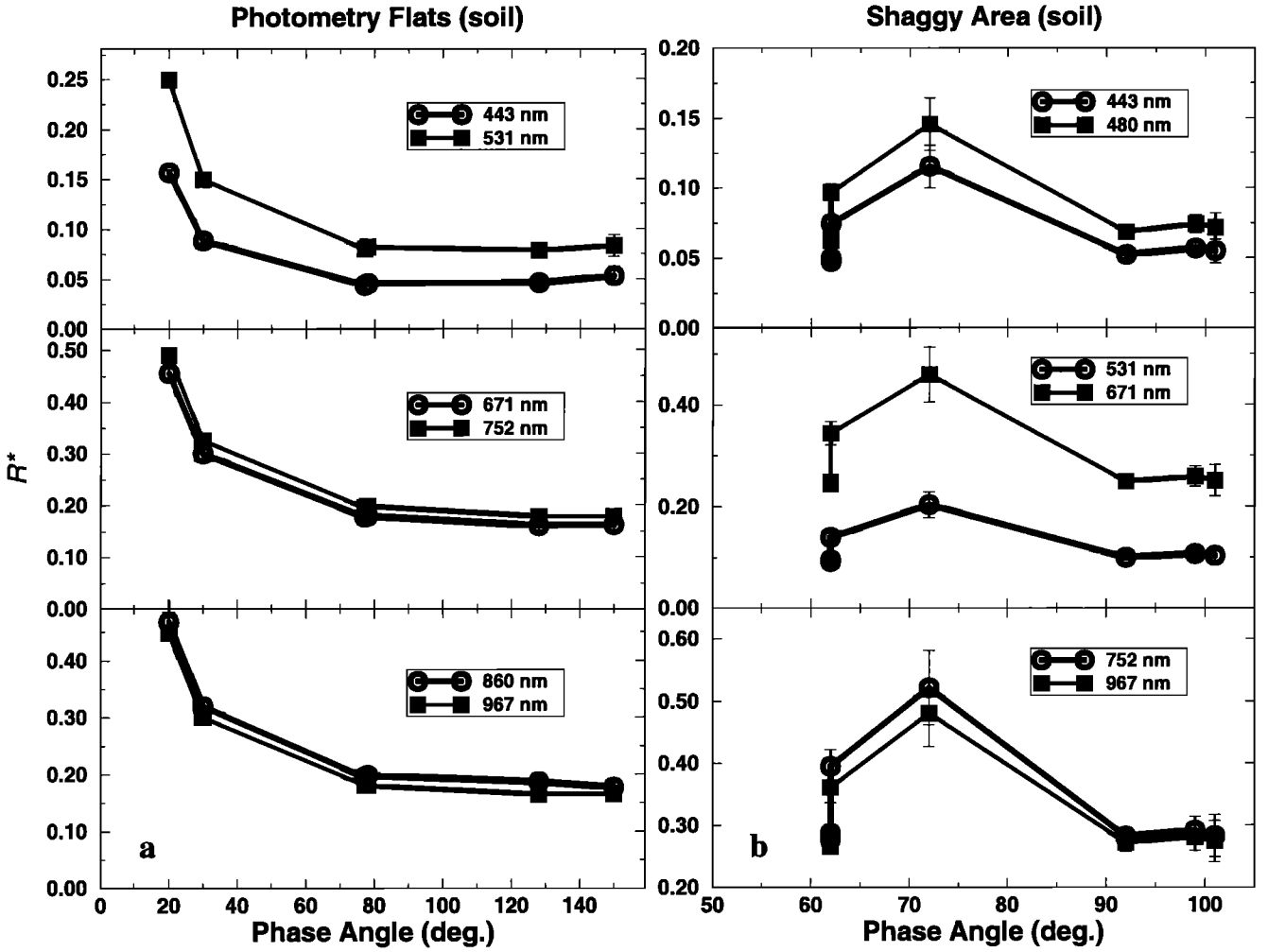

Figure 5. Phase curves at six wavelengths for soils at the (a) Photometry Flats and (b) Shaggy area photometric spot locations. Error bars represent standard deviation of sampled regions. Peak in R^* at 72° for Shaggy phase curves may be due to specular reflection. See Figure 2 for locations.

Thus we determined the wavelength with the lowest least squares residual and chose its θ–bar and h values to use as constants for all wavelengths in subsequent model runs (Tables 2-4). In all cases, the 443 nm band exhibited the smallest residuals. Error estimates for each parameter represent their variations in the 10 best fits to the model.

The θ–bar parameter represents the average of surface facet tilts at scales from the wavelength of light to the centimeter-scale resolution of the IMP images, i.e., the "macroscopic roughness" [cf. *Hapke,* 1993]. Although it is intuitive that θ–bar should not vary with wavelength, it could be argued that illumination of shadowed regions by diffusely scattered light from the atmosphere or surface may cause an apparent decrease in the surface roughness. Whether such diffuse light can brighten shadows sufficiently to affect the apparent surface roughness at the ~millimeter scale is uncertain. In such a case, θ–bar would represent a lower limit for surface roughness. Alternatively, the presence of deep absorption bands at specific wavelengths could explain variations in θ–bar; however, no major absorption bands have been seen in the IMP spectra (with the exception of the broad Fe^{3+} absorption shortward of 750 nm) [e.g., *J.F. Bell III et al.,* submitted paper, 1999; *McSween et al.,* this issue]. Thus we maintain a constant θ–bar value with wavelength in the model runs.

Other scattering models were considered besides that of Hapke (e.g., Minnaert, lunar-Lambert [*Minnaert,* 1941; *McEwen,* 1991], Lommel-Seeliger [*Hapke,* 1993], or Kubelka-Munk [*Barron and Torrent,* 1986]), but the Hapke model was preferred due to the available viewing geometries and relatively high albedo nature of these data sets (compared to dark asteroids or lunar maria).

4.1. Photometric Spots

The small range of phase angle coverage for the Mermaid Dune and Shaggy area photometric spots precludes meaningful Hapke modeling of their phase curves. However, the four surface types sampled in the Mermaid data allow a qualitative comparison of phase curves to determine relative surface properties. *Helfenstein and Veverka* [1987] used ratio plots of phase curves to distinguish large-scale roughness, opposition effects, or particle phase function differences

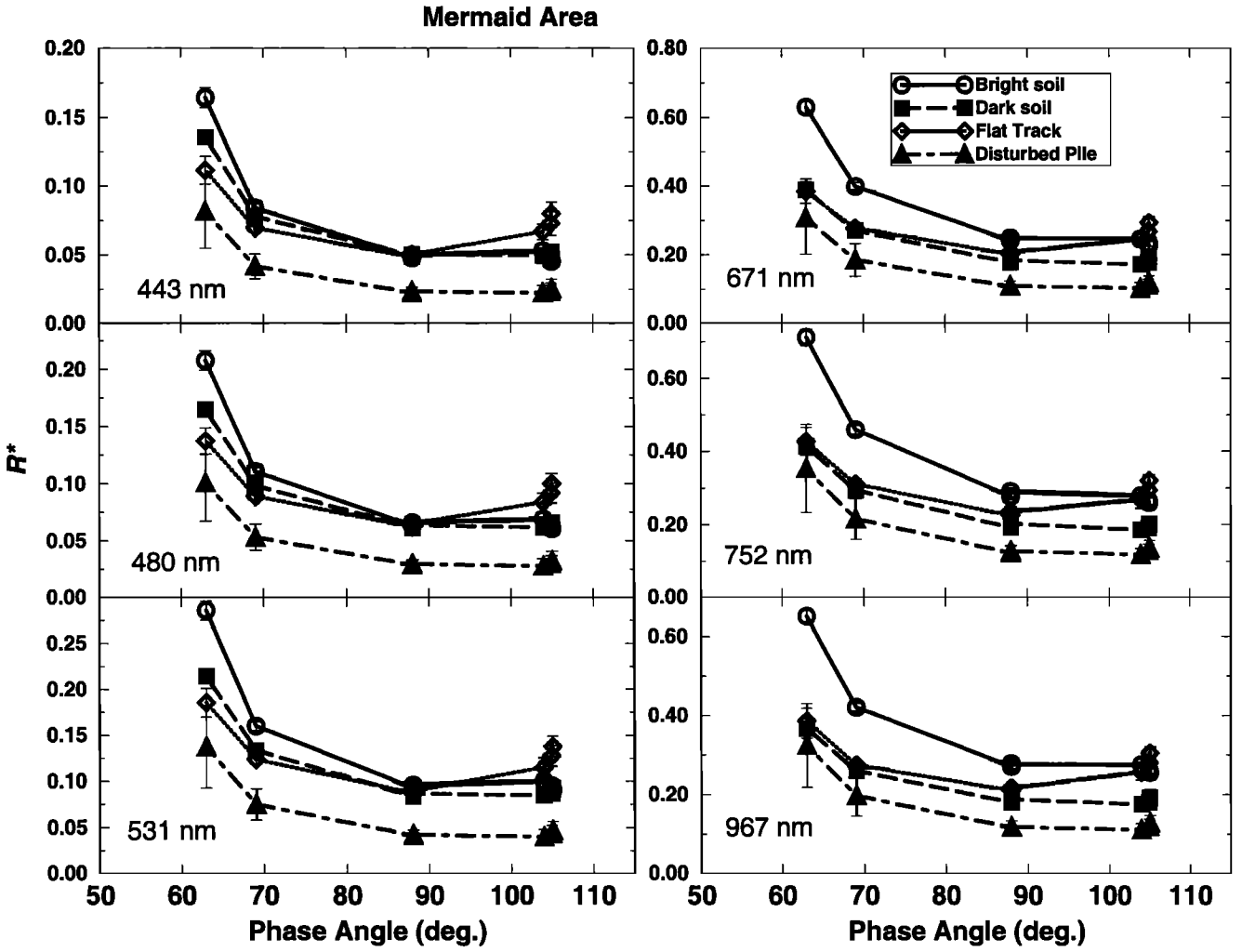

Figure 6. Phase curves at six wavelengths for four materials at the Mermaid dune photometric spot. Flat Track and Disturbed Pile are surfaces disturbed by the rover wheels. Error bars represent standard deviation of sampled regions. See Figure 2 for locations.

among materials. At high phase angles, macroscopically rougher surfaces cast more shadows toward the observer than smoother surfaces, causing a decrease in forward scattering [cf. *McGuire and Hapke,* 1995]. As such, phase curve ratios of smooth/rough surfaces exhibit a positive slope with increasing phase angle. Six phase curve ratios shown in Figure 8 compare the four Mermaid surface materials at 752 nm. Qualitatively, it appears that the materials increase in macroscopic roughness from flat track → dark soil → bright soil → disturbed pile, although differences between dark and bright soil are minimal. This ordering makes intuitive sense and provides an independent confirmation of the internal consistency of the phase curve data.

The Photometry Flats spot covers phase angles from 20° to 150° (Table 1a), which provides sufficient phase coverage to permit Hapke modeling, although with limited constraints on the opposition effect parameters. Results for each wavelength are shown in Table 2 and are discussed below.

4.2. Photometric Equator

As described above, the photometric equator data were analyzed by extracting spectra for four specific material units, thereby increasing the phase angle coverage and providing better constraints for Hapke modeling. In Figure 9, ratios of cubic polynomial fits to the phase curves of these four units are shown at 752 nm for phase angles from 4° to 135° (the common phase angle range among the four units). These fits suggest interesting variations that can be qualitatively interpreted in a manner similar to that used for the Mermaid photometric spot materials (Figure 8). Although the nonlinear trends in Figure 9 suggest that the effective roughness of a given surface varies with phase, we interpret this as an artifact of the cubic polynomial fit. These ratio curves are meant only as schematic representations of the relative differences among the phase curves. We interpret them based on overall trends, i.e., ratios of smooth/rough surfaces exhibit a positive slope with increasing phase angle, particularly at higher phase angles. As such, their trends suggest that the four units increase in macroscopic roughness from gray rock → bright soil → dark soil → red rock, with little difference between the dark soil and red rock.

The Hapke model was used for each of the four units at the three available wavelengths. Results are presented in Table 3 (soil units) and Table 4 (rock units) and discussed below.

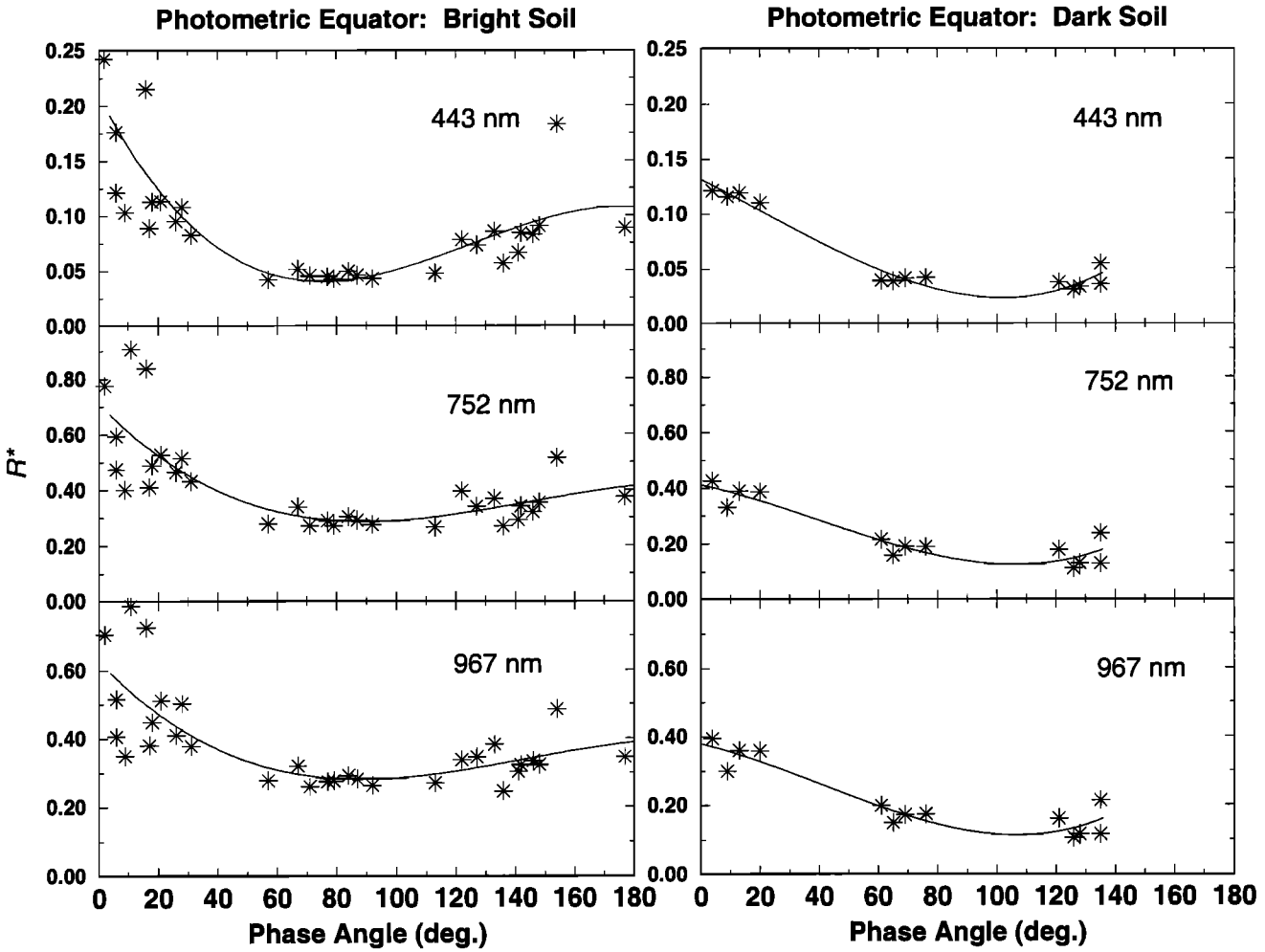

Figure 7. Phase curves at three wavelengths for four units obtained from entire photometric equator sequence: (a) soils and (b) rocks. Curve is cubic polynomial fit to phase points to provide qualitative measure of phase curve trends. See Figure 3 for locations of units.

4.3. Discussion of Hapke Modeling Results

The results of the Hapke modeling of Photometry Flats and the photometric equator units in Tables 2-4 can be analyzed for overall systematic deviations by comparing ratios of the observed to predicted (calculated) R^* values. Figure 10 shows these ratios for the five materials modeled. For Photometry Flats the few phase angle points (six) result in only small differences between the Hapke model and the actual values. For the photometric equator materials, stronger deviations from unity are observed, which may arise due to the increased variability of each data set resulting from the selection method discussed above. The red rock has particularly high ratio values at phase angles > 170°, which may result from unintentional sampling of shadowed materials at higher phase.

As discussed by several workers [e.g., *Helfenstein and Veverka,* 1987; *Mustard and Pieters,* 1989; *McEwen,* 1991], the parameters of the Hapke model are strongly coupled and can provide mathematically reasonable solutions even for parameters that are poorly constrained by the data. For example, the θ–bar values calculated for the photometric equator rocks and soils (Tables 3-4) are nearly equal and very small (of the order of terrestrial snow [cf. *Domingue et al.,* 1997]), whereas the θ–bar values for the Photometry Flats spot are somewhat higher. While this may indicate real differences in surface roughness, it may also be that the differences in the phase angle coverage and variability in the data sets are responsible.

Previous estimates of photometric parameters using an earlier version of the Hapke model were derived from Viking Lander 1 data for "dust" by *Arvidson et al.* [1989a] for blue (400-520 nm), green (500-590 nm), and red (600-740 nm) wavelengths. In Figure 11, their single scattering albedo (w) values are compared to those presented in this work (Tables 2-4) and to those from *Guinness et al.* [1997b], who presented results from a modified version of a Hapke model using Viking lander data for rocks and soils in the red wavelength band. The *Arvidson et al.* [1989a] results are higher than those derived here for all materials, while the *Guinness et al.* [1997b] values for rocks and soils are similar to our bright soil materials at comparable wavelengths.

Clancy and Lee [1991] found that a w value of 0.92 best modeled the atmospheric dust using Viking Infrared Thermal Mapper (IRTM) data, although this pertains to the integrated

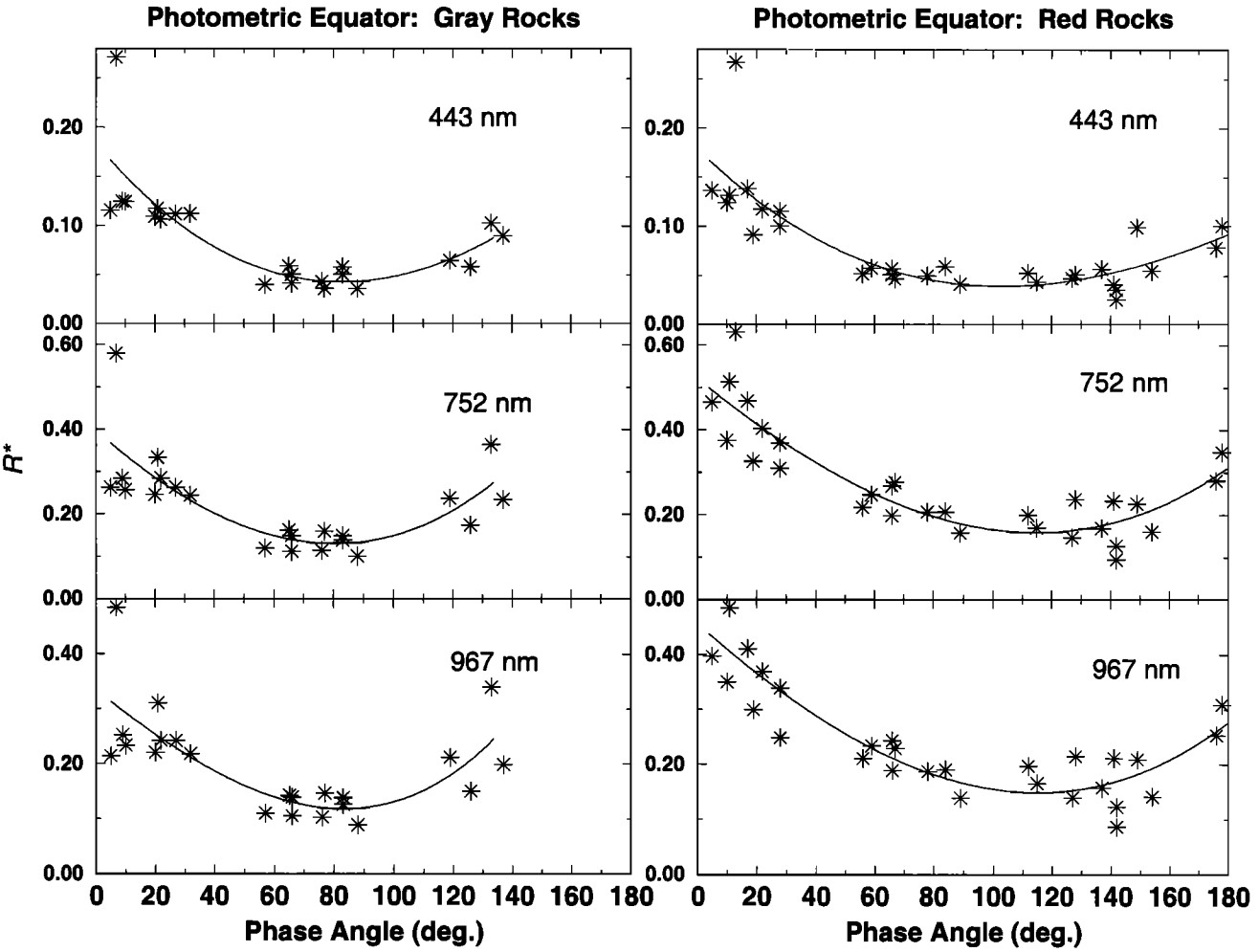

Figure 7. (continued)

solar flux over the wavelength region 300-3000 nm. *Pollack et al.* [1979] obtained a value of 0.86 for atmospheric dust using Viking lander data (averaged over 400-1100 nm), while *Pollack et al.* [1995] reported a value of 0.93-0.94 for the 600-740 nm band. All these values are greater than our maximum value of 0.73 for the bright soils at 752 nm (Table 3) but similar to the IMP results for atmospheric dust given by *Tomasko et al.* [this issue].

The *Arvidson et al.* [1989a] θ–bar values (5.3°-6.4°) for Viking "dust" are intermediate between the soils presented here (Tables 2-3) . Their opposition effect widths (h) (0.125, 0.136, and 0.173, for the blue, green, and red wavelengths, respectively) are similar to the dark soil and Photometry Flat soils. The *Guinness et al.* [1997b] h parameter value for rocks (0.13) is greater than either of our rock units, and their soil value (0.14) is more similar to our dark soil unit and Photometry Flats. Their θ–bar value for rock (8.9°) is close to the Photometry Flats value, but their soil value (26.8°) is much greater than all our materials. Such differences likely result from a combination of variations between (1) the actual surface materials between the SMS and Viking lander sites; (2) the precision of the multispectral data sets; and (3) the specific application of Hapke theory in the models used.

Comparison of the single particle scattering function

Table 2. Hapke Scattering Model Parameters for Photometry Flats Soil

Parameter	443 nm*	531 nm	671 nm	752 nm	860 nm	967 nm
w	0.16 ± 0.03	0.29 ± 0.03	0.52 ± 0.03	0.56 ± 0.03	0.56 ± 0.03	0.53 ± 0.03
b_0	0.995 ± 0.05	0.29 ± 0.13	0.025 ± 0 05	0.015 ± 0.05	0 010 ± 0.05	0.015 ± 0.05
h	0.170 ± 0.007	0.170 ± 0.007	0.170 ± 0.007	0.170 ± 0.007	0.170 ± 0.007	0.170 ± 0.007
b	0.145 ± 0.040	0.190 ± 0.040	0 213 ± 0.040	0.208 ± 0.040	0.195 ± 0.040	0.203 ± 0.040
c	1.000 ± 0.040	1.000 ± 0.040	1.000 ± 0.040	1.000 ± 0.040	1.000 ± 0.040	1.000 ± 0.040
θ–bar	8 ± 2	8 ± 2	8 ± 2	8 ± 2	8 ± 2	8 ± 2

Here, w, single scattering albedo; b_0, opposition effect amplitude; h, opposition effect width; b, c, single particle scattering function parameters; θ–bar, macroscopic roughness parameter.

* The θ–bar and h parameters were obtained using 443 nm preliminary run results.

Table 3. Hapke Scattering Model Parameters for Photometric Equator: Bright, Dark Soils

	Bright			*Dark*		
Parameter	443 nm*	752 nm	967 nm	443 nm*	752 nm	967 nm
w	0.19 ± 0.02	0.73 ± 0.02	0.71 ± 0.02	0.16 ± 0.02	0.53 ± 0.02	0.50 ± 0.02
b_0	1.00 ± 0.05	0.37 ± 0.05	0.24 ± 0.05	1.00 ± 0.05	0.73 ± 0.05	0.66 ± 0.05
h	0.062 ± 0.010	0.062 ± 0.010	0.062 ± 0.010	0.100 ± 0.004	0.100 ± 0.004	0.100 ± 0.004
b	0.285 ± 0.020	0.113 ± 0.020	0.095 ± 0.020	0.200 ± 0.020	0.178 ± 0.020	0.183 ± 0.020
c	0.522 ± 0.020	0.997 ± 0.020	1.000 ± 0.020	0.925 ± 0.040	1.000 ± 0.040	1.000 ± 0.050
θ–bar	4 ± 2	4 ± 2	4 ± 2	2 ± 2	2 ± 2	2 ± 2

Here, *w*, single scattering albedo; b_0, opposition effect amplitude; *h*, opposition effect width; *b*, *c*, single particle scattering function parameters; *θ*–bar, macroscopic roughness parameter.

*The *θ*–bar and *h* parameters for both soils were obtained using 443 nm preliminary run results.

parameters *b* and *c* has often been used to assess the general scattering behavior of materials [e.g., *Mustard and Pieters,* 1989; *Domingue and Hapke,* 1992; *McGuire and Hapke,* 1995; *Domingue et al.,* 1995, 1997]. *McGuire and Hapke* [1995] described the *b* parameter as giving the angular width of each lobe of the single scattering function, and the parameter *c* as giving the amplitude of the backscattered lobe compared to the forward lobe. In the parameter space of *Domingue et al.* [1995, 1997], a *c* value < 0.5 implies a predominantly forward scattering material, and a value > 0.5 corresponds to a backscattering material. *McGuire and Hapke* [1995] studied the intensity and polarization of light scattered by several centimeter-sized artificial particle types as a function of wavelength and found that particles with different shapes and roughness populate discrete regions of *b*-*c* space, forming an L-shaped pattern related to deviations from a particle's spherical and internal perfection. Their particles are plotted as a function of *b* and *c* in Figure 12 (with *c* values converted to be consistent with the model results used here (cf., *Domingue et al.,* [1995, 1997])) along with the scattering parameters from the photometric equator units and the Photometry Flats spot. Smooth, clear spheres plot farthest to the right on the plot, corresponding to a highly forward scattering regime. With greater particle surface roughness (at the scale of the observation wavelength) and/or internal inhomogeneities (scatterers such as microcracks, inclusions, or vesicles), the *b* value decreases (becoming constant around 0.25) as the *c* value increases. *Hartman and Domingue* [1998] noted that centimeter-sized particles are not typical of most planetary regoliths, but also showed that the *McGuire and Hapke* [1995] scattering functions are not significantly different from the behavior of the larger particles when scaled to smaller particle sizes. In Figure 12, note that the soils and red rocks cluster at high *c* values, near materials with a high density of internal scatterers. It is uncertain at this time why one bright soil point (443 nm) plots closer to the region with a moderate density of scatterers. Most intriguing are the gray rock points, which plot at lower *c* values in the region characterized by agglutinates and rough, clear spheres. This may represent a glassy or varnished surface present on the gray rocks, as discussed below.

4.4. Photometric Effects on Observed Spectra

Results of photometric parameter modeling may be better understood when placed in the context of empirical data, i.e., spectra of surface materials. A large part of the Pathfinder mission operation strategy involved obtaining low-compression images using many or all of the IMP filters. At the beginning of the mission, small (64x64 pixel) subframes (referred to as "multispectral spots") were obtained in 12 filters of regions of interest, usually between 0900 and 1200 LTST. Later, the Superpan data set [cf. *Gaddis et al.,* this issue] provided 15-band images of much of the landing site, obtained between 0900-1000 and 1430-1530 LTST. Spectra have been extracted from both data sets for 37 rocks and five soils to determine empirically the effects of viewing geometry on spectral response. Although the results vary, typical spectra are shown at the top of Figure 13 for the rock nicknamed "Shark" and an undisturbed soil near Yogi. Times

Table 4. Hapke Scattering Model Parameters for Photometric Equator: Gray, Red Rocks

	Gray			*Red*		
Parameter	443 nm*	752 nm	967 nm	443 nm*	752 nm	967 nm
w	0.20 ± 0.02	0.51 ± 0.02	0.47 ± 0.02	0.18 ± 0.02	0.57 ± 0.02	0.53 ± 0.02
b_0	0.99 ± 0.05	0.41 ± 0.05	0.16 ± 0.05	1.00 ± 0.05	0.38 ± 0.05	0.18 ± 0.05
h	0.054 ± 0.005	0.054 ± 0.005	0.054 ± 0.005	0.068 ± 0.006	0.068 ± 0.006	0.068 ± 0.006
b	0.348 ± 0.020	0.375 ± 0.020	0.363 ± 0.020	0.205 ± 0.020	0.178 ± 0.020	0.173 ± 0.020
c	0.432 ± 0.020	0.367 ± 0.020	0.397 ± 0.020	0.870 ± 0.020	1.000 ± 0.020	1.000 ± 0.050
θ–bar	4 ± 2	4 ± 2	4 ± 2	4 ± 2	4 ± 2	4 ± 2

Here, *w*, single scattering albedo; b_0, opposition effect amplitude; *h*, opposition effect width; *b*, *c*, single particle scattering function parameters; *θ*–bar, macroscopic roughness parameter.

*The *θ*–bar and *h* parameters for Gray rocks were obtained using 443 nm preliminary run results.

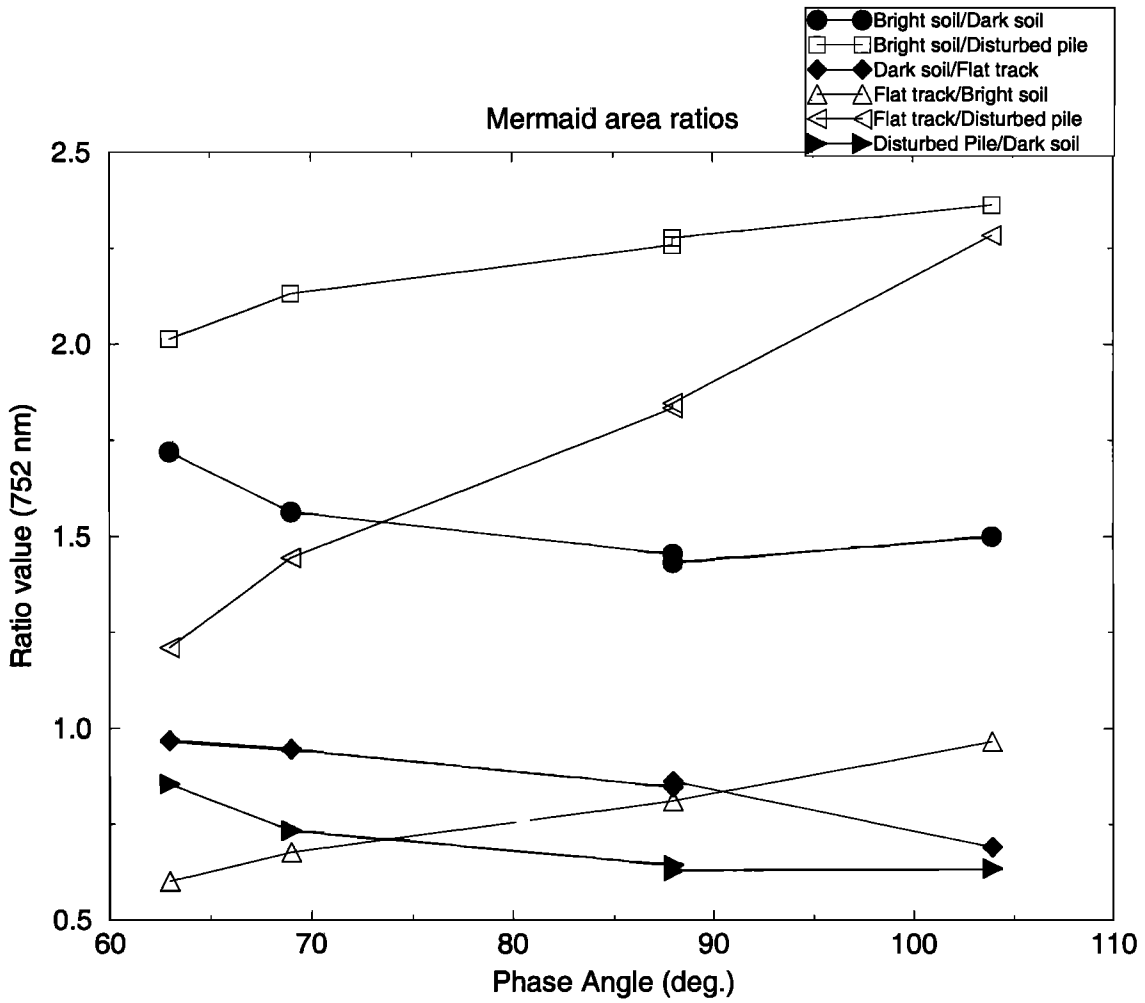

Figure 8. Phase curve ratios (at 752 nm) for materials from Mermaid photometric spot data. Overall positive slopes with increasing phase angle (open symbols) suggest that the material in the ratio numerator has a smoother surface than the material in the denominator. Flat rover tracks appear smoothest of the four materials.

of acquisition, incidence, and phase angles are shown next to each spectrum. These spectra are composed of left- and right-eye spectra which have been multiplicatively scaled to a common value at 671 nm to account partially for minor left/right-eye differences in R^* that resulted from small, inherent viewing geometry offsets of the on-board calibration targets between the IMP eyes [cf. *McSween et al.*, this issue, *J.F. Bell III et al.*, submitted paper, 1999; *Reid et al.*, this issue]. The ratio of the multispectral spot/Superpan spectra are shown below each spectra pair. The ratios are relatively flat with a slight downturn in the blue wavelengths. Also shown above the Shark ratio in Figure 13 is the average multispectral spot/Superpan ratio for all 42 measurements, which is also relatively flat, with some indication of a downturn <600 nm. This suggests that the overall R^* value will be the major change expected between spectra taken at two different times of day (assuming similar atmospheric opacity conditions between measurements). The blue downturn could be a bias resulting from the data set being dominantly composed of rocks from the Rock Garden (west of the lander), for which the Superpan imaging data were obtained at ~0930 LTST. Most of these east-facing rock facets were directly illuminated at that time of day, resulting in a proportionally greater direct/diffuse radiant flux ratio and hence greater reflectance in the blue wavelengths, as described by *Thomas et al.* [this issue] and *Reid et al.* [this issue]. However, the additional presence of the downturn in the flat-lying Yogi soil data could imply an actual wavelength dependence to the photometric function, acting as a second-order effect.

5. Discussion and Conclusions

Reflectance spectroscopy studies of Mars surface materials have provided important mineralogical, chemical, and surface property information vital to constraining the geologic, climatic, and weathering history of Mars [e.g., *Singer et al.*, 1979; *Soderblom*, 1992; *Banin et al.*, 1992; *Gooding et al.*, 1992; *Bell et al.*, 1990, 1993; *Bell and Crisp*, 1993; *Roush et al.*, 1993; *Singer and McSween*, 1993; *Bishop et al.*, 1995]. Understanding how the photometric properties of Martian rocks and soils affect their reflectance spectra is a crucial component of these studies. The photometric imaging sequences obtained by the IMP camera provide a valuable

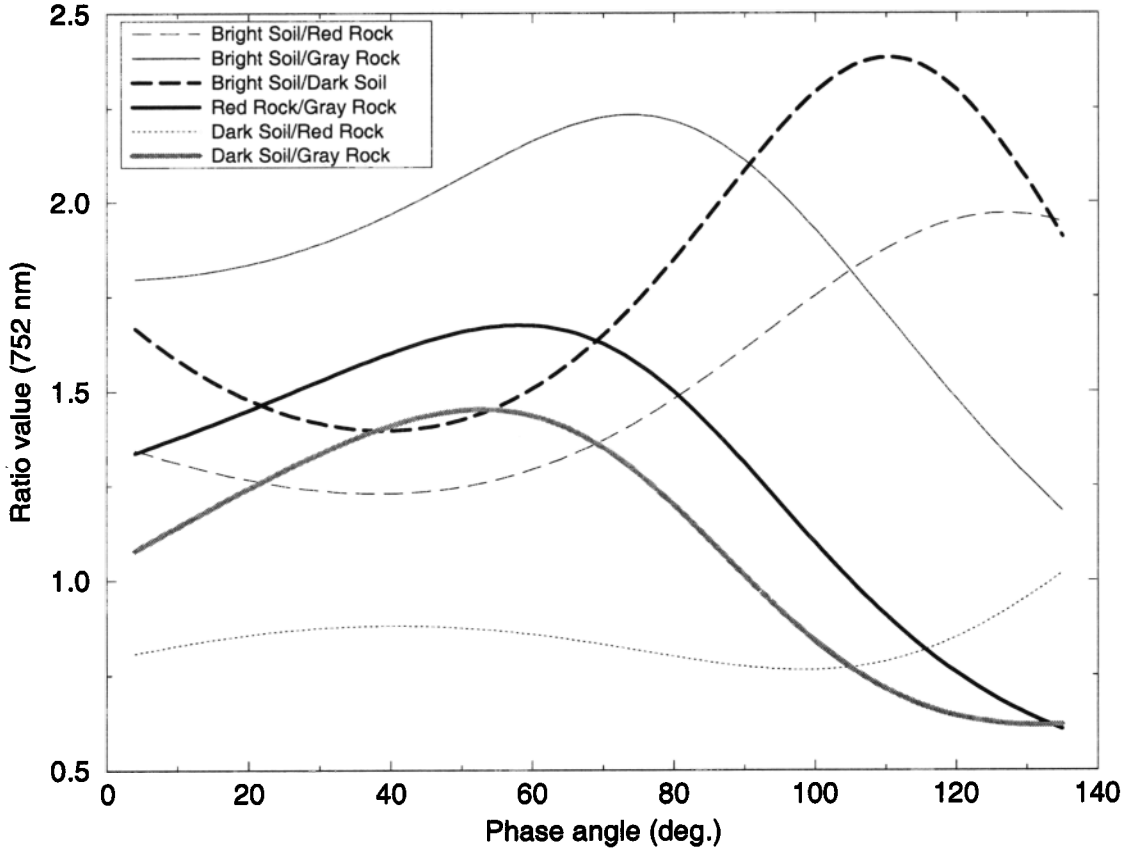

Figure 9. Ratios of cubic polynomial fits to phase curves (at 752 nm) for four units from photometric equator data. Overall positive slopes with increasing phase angle suggest that the material in the ratio numerator has a smoother surface than the material in the denominator. Gray rocks appear smoothest (solid lines).

data set with which to study spectral photometry of materials from a landing site perspective. Although the photometric functions and parameters presented here include uncertainties (due to a combination of data set variability, available phase angle coverage, and the current state of radiometric and spectral calibration), preliminary conclusions can be made regarding the photometric properties of rocks and soils at the SMS.

The photometric functions of the materials studied here are dominantly backscattering, in agreement with results from Viking lander data [e.g., *Guinness*, 1981; *Guinness et al.*, 1987, 1997a,b; *Arvidson et al.*, 1989a,b]. Some materials exhibit an additional forward scattering component, particularly the gray rock unit (Figure 7b). The soil units show less photometric variability than the rock units, although the Mermaid area soils qualitatively show the smoothing and roughening effects of rover wheel activity (Figure 8). Unfortunately, phase angle coverage for the Mermaid area is not sufficient for Hapke modeling. The Photometry Flats area has a greater range of phase angles, although the few phase points lead to uncertainty in the accuracy of the results, particularly for the opposition effect parameters b0 and h.

The opposition effect amplitude (b0) is physically related to the opacity of particles; a value of 1.0 implies that all light is scattered at the surface and the particle is opaque [e.g., *Domingue et al.*, 1997]. For all the materials modeled here, b0 decreases with increasing wavelength, which is consistent with the idea that these materials are more opaque (more surface scattering) in the blue wavelengths and become more transparent (more internal scattering) in the red [cf. *Domingue and Hapke*, 1992]. However, *Hillier* [1997b] observes that composite particles with internal scatterers (such as the aggregates deposited on the Pathfinder lander magnetic targets [*Hviid et al.*, 1997] or the aolian bright soil materials) may not be well modeled using radiative transfer models due to variation in close packing.

Although the opposition width parameter h is weakly constrained by the Hapke scattering model in these data sets (Tables 2-4), it appears that this value on average increases from gray rock → bright soil → red rock → dark soil units. The parameter h is physically related to porosity and particle size distribution [*Hapke*, 1986, 1993]. Large values of h correspond to a less porous material and/or to lower ratios of largest-to-smallest particle size (depending on the assumed particle size power law distribution) [cf. *Helfenstein and Veverka*, 1987; *Hapke*, 1993]. Thus the relatively larger h values for the dark soil and Photometry Flats materials may imply materials with lower porosity and/or a more uniform particle size distribution. Conversely, the low h values of the gray rock unit would correspond to materials with high porosity and/or a broader particle size distribution. This is consistent with the vesicular nature observed on many gray rock surfaces [cf. *McSween et al.*, this issue].

Comparison of the single scattering function parameters b

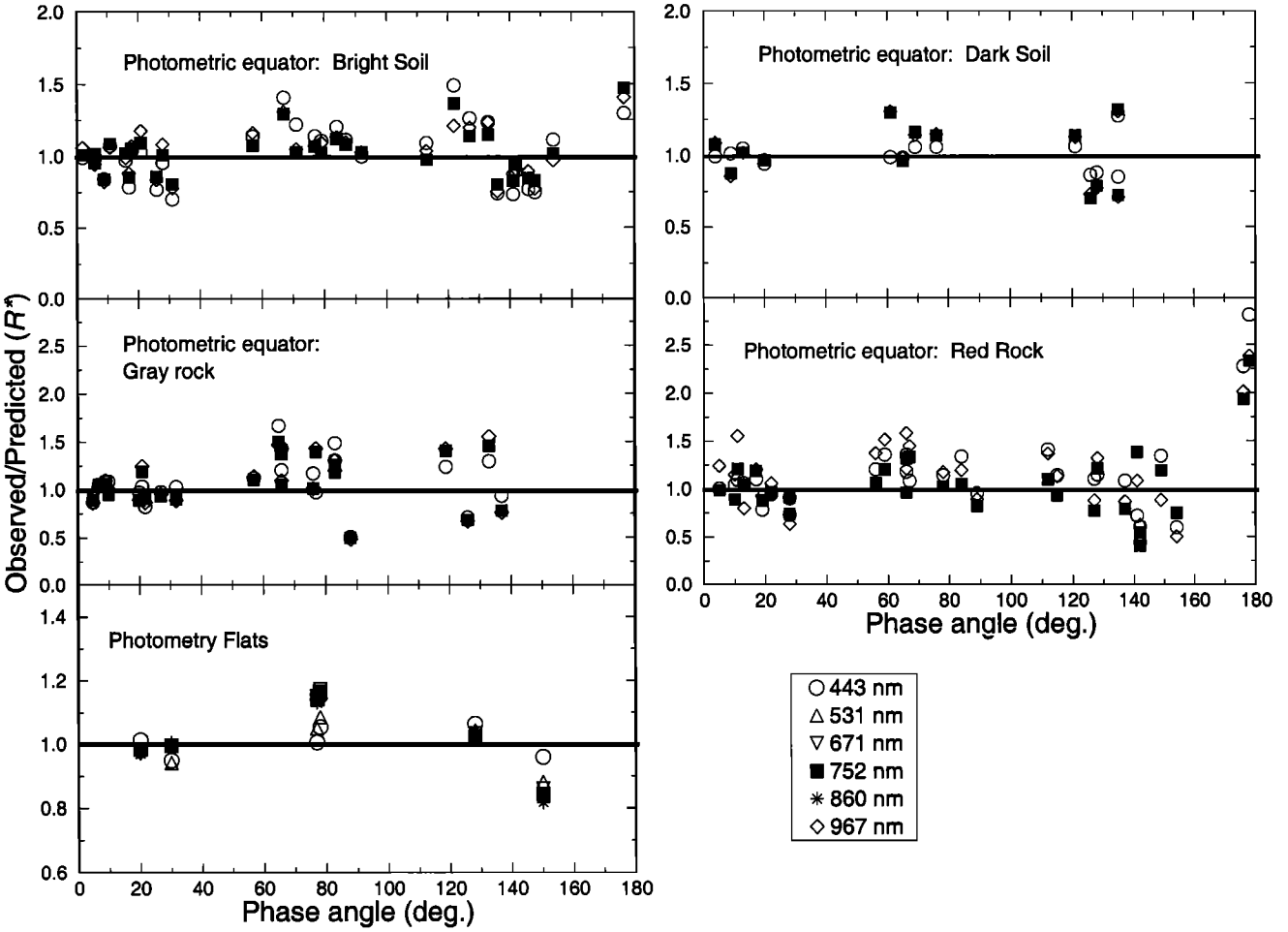

Figure 10. Ratios of observed R^* values to those predicted (calculated) from the Hapke scattering model for the four photometric equator units (three wavelengths) and Photometry Flats (six wavelengths). Solid line at 1.0 represents perfect agreement between data and model.

and c (Figure 12) suggests that the gray rocks are unique among the materials studied here and have surfaces composed of "rough, clear, agglutinate-like" particles with no internal scatterers at the wavelength scale [*McGuire and Hapke,* 1995; *Hartman and Domingue,* 1998]. On the basis of qualitative phase curve comparisons (Figure 9), the gray rock unit also appears to have the smoothest surface (at ~millimeter to centimeter scales) among the four photometric equator units, although the macroscopic roughness (<centimeter-scale) θ–bar values are relatively similar statistically for all units (Tables 2-4).

Thus the derived Hapke parameters suggest that the gray rock surfaces may have photometric properties consistent with higher porosity (very fine (~millimeter) vesicularity?) and macroscopically smoother surfaces than the soils or red rocks and may be composed of clear, agglutinate-like particles that are rough at the wavelength scale. This is consistent with the theory that most rocks free from obvious dust contamination on Mars reveal a smooth coating similar to terrestrial varnished rock surfaces [*Guinness et al.,* 1996, 1997a,b; *Israel et al.,* 1997]. Alternatively, the coating may be indicative of an impact-derived glassy rind, similar to that postulated by *Schultz and Mustard* [1998] based on laboratory reflectance spectra of terrestrial impact melts.

For comparison, red rocks may have less porous surfaces that are slightly macroscopically rougher (Figure 9) and composed of more irregularly shaped particles with more internal scatterers (Figure 12). If red rocks are simply gray rocks with a weathered and/or aolian-deposited coating of soil-like materials, then the lower porosity of red rock surfaces could be consistent with an in-filling of the small vesicles in the higher-porosity gray rock surfaces. However, such deposition should make the red rock surfaces macroscopically smoother than the gray rocks. Based on Figure 9, this does not appear to be the case. It may be that irregular cementation, weathering, and/or "drifts" of soil-like materials increase roughness from gray → red rocks.

Also based on Figure 9, the dark soils appear to be macroscopically rougher than bright soils (as opposed to the statistically similar θ–bar values in Table 3). If this is the case, coating effects could also explain the soils' photometric parameters, in which the dark soil is also less porous than the bright soil (an observation consistent with the rover wheel tests on both soil types [*Rover Team,* 1997]). As dark soil is coated with bright "dust," the topography would become more subdued and surface porosity would increase (like that of the bright soil) because of low-density surfaces created via airfall deposition. The "roughening" experienced by the gray

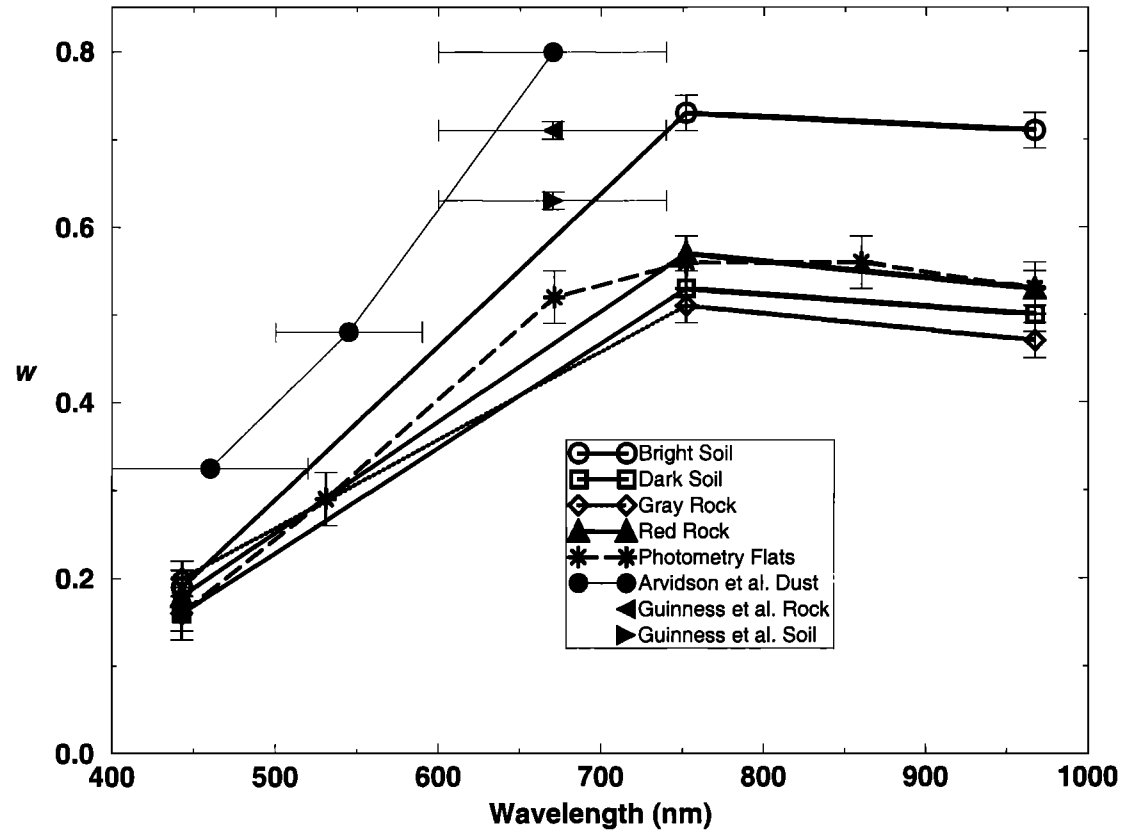

Figure 11. Single scattering albedo (w) values derived for materials modeled here, for Viking lander "dust" soil material from *Arvidson et al.* [1989a], and rock and soil units from *Guinness et al.* [1997b]. Horizontal bars represent filter bandwidths of the Viking lander images. Vertical error bars are standard deviations of w values.

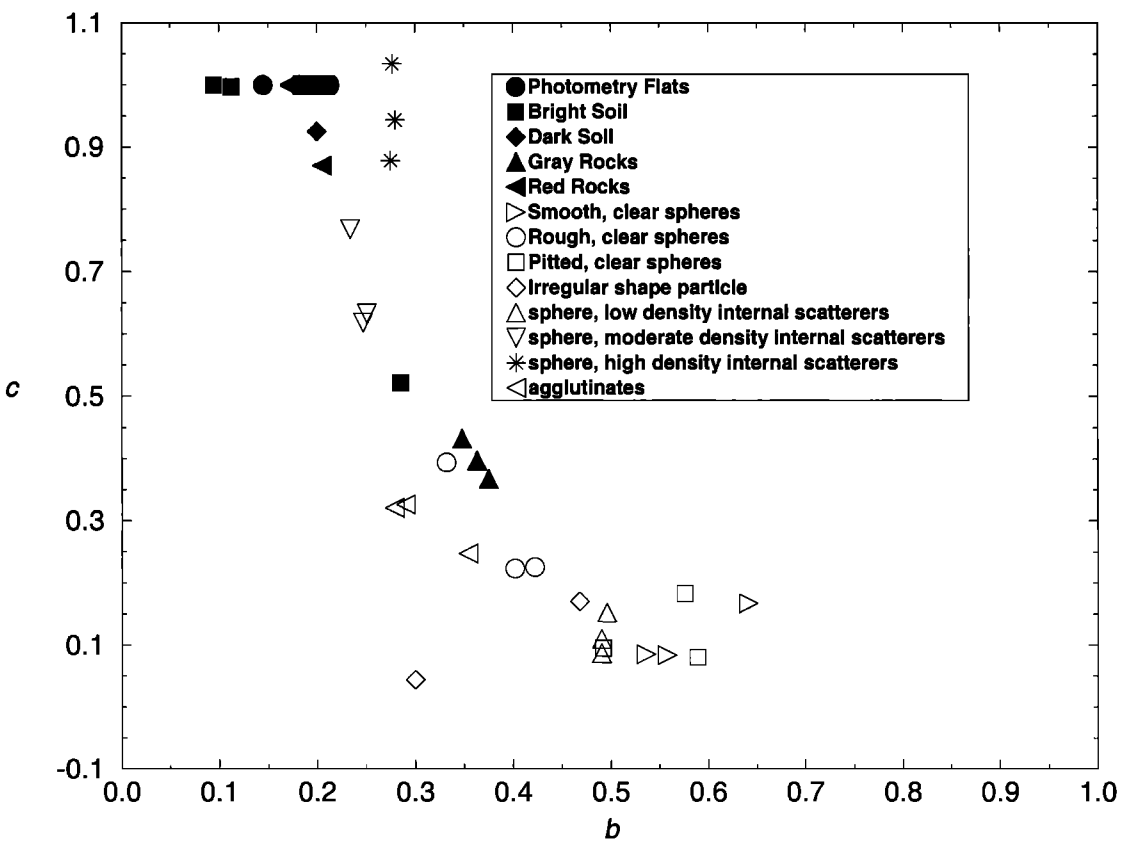

Figure 12. Correlation between single scattering parameters b and c (derived from a double Henyey-Greenstein function) for four photometric equator units and Photometry Flats. Also included are parameter values derived for artificial particles of various smoothness, sphericity, and internal scatterers [*McGuire and Hapke*, 1995] from *Domingue et al* [1997] Note that the gray rock values cluster in the "rough, clear spheres" and "agglutinates" region.

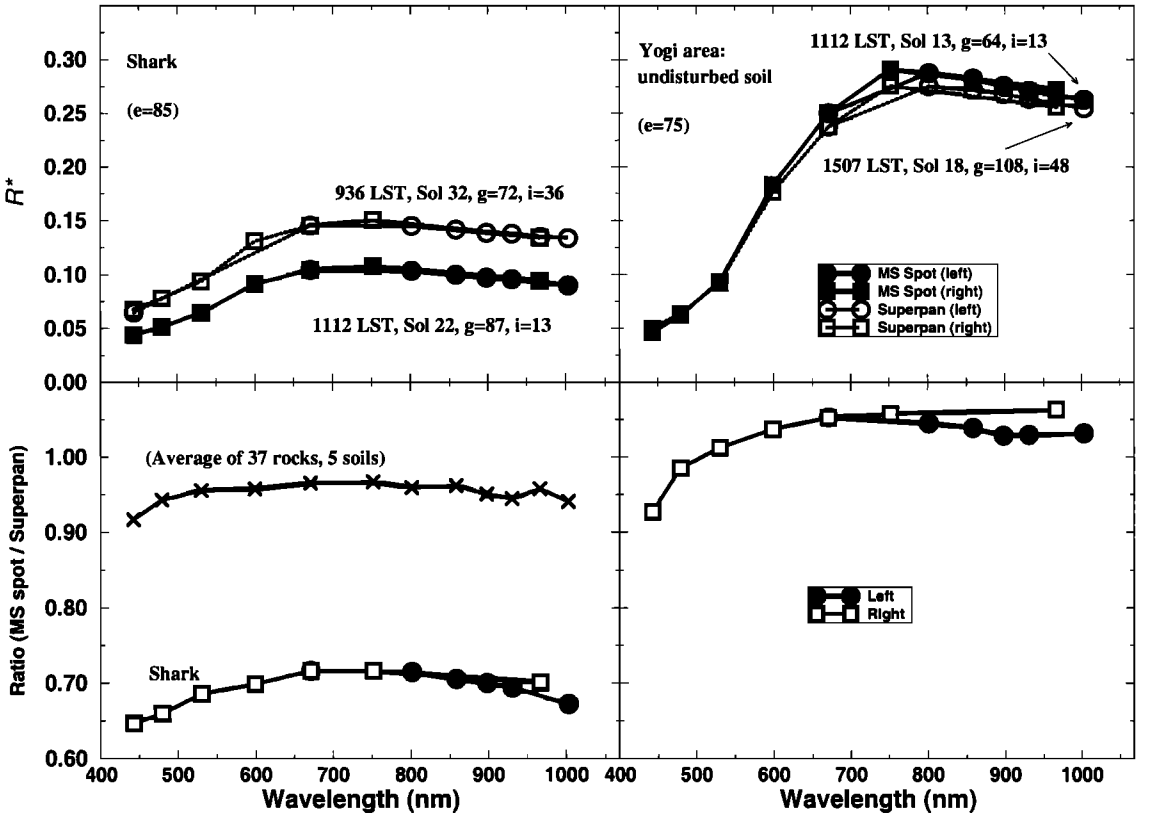

Figure 13. (top) Spectra obtained from the same location on the rock "Shark" and an undisturbed soil near Yogi using multispectral spot and Superpan data obtained on different times of day (and sols) from left- and right-eye filters. Also shown are the emission (e), incidence (i), and phase (g) angles. (bottom) Ratios of multispectral spot/Superpan spectra, demonstrating the relatively flat nature of the spectral differences between data obtained at different times of day, with the exception of an apparent downturn at wavelengths lower than 600 nm. Also shown with the Shark ratio spectrum is the average ratio of multispectral spot/Superpan spectra for 37 rocks and five soils, showing a similar trend. Variations on ratio values are of the order of the data point size (i.e., <5%).

→ red rock transition may not likewise occur during the dark → bright soil transition because the dark soil is already more compacted (lower porosity) and more subject to even distribution of airfall dust than the higher porosity gray rock surfaces.

The single scattering albedo w is the most well-constrained parameter in the Hapke model results presented here (Figure 11). The bright soils have the highest albedo in the red and near-infrared, the gray rocks have the highest 443 nm albedo, and the red rock albedos are intermediate. The w values for Photometry Flats are similar to the red rocks in the near-infrared and more like the dark soil at 443 nm (Tables 2-4). This suggests that some units may represent mixtures of one or more units. Adopting the theory that mixing models are linear when the reflectances are expressed as single scattering albedo [cf. *Mustard and Pieters,* 1989; *Hapke,* 1993], the quantitative nature of the coatings thought to be responsible for the "reddened" spectral character of the red rock unit can be investigated [cf. *McSween et al.,* this issue]. A simple three-component "unmixing" model (available in ISIS [cf. *Eliason,* 1997]) was used with the single scattering albedo "spectra" (Figure 11) to determine the percentage of bright soil, dark soil, and gray rock end-members required to model the red rock albedo spectrum. The results showed that the red rock albedo can be modeled (to within <2% error) by relatively large amounts of dark soil (43%) and bright soil (21%) covering 36% gray rock. This is consistent with the reflectance spectra mixture modeling done by *McSween et al.* [this issue] that shows red rocks are well-modeled by a combination of 40% dark substrate and 60% of an optically thick ferric powder coating. It is recognized that more sophisticated models of multicomponent surfaces may be more appropriate than this simple mixing method [e.g., *Hillier,* 1997a; *Clark,* 1998], but this exercise does suggest that the red rock materials are likely contaminated by soil materials deposited on gray rocks.

Because of operational constraints, the majority of IMP images used to extract spectral information were obtained between 0900 and 1530 LTST, resulting in intermediate phase angles for most surfaces (e.g., 45-130°) where differences in reflectance are less variable than at extreme phase. Figure 13 shows that the greatest difference between spectra obtained at separate times of day is in overall R^* value. However, small spectral differences in the blue wavelengths may indicate either a wavelength-dependent photometric function or the result of residual diffuse/direct lighting uncertainties in the current version of the calibration [*Reid et al.,* this issue; *Thomas et al.,* this issue].

Future analyses of the IMP photometric imaging sequences will benefit from the next version of the IMP calibration algorithm, which will incorporate improved corrections for the photometric function of the calibration targets, atmospheric opacity variations, and the effects of direct/diffuse flux [*Reid et al.*, this issue]. Completion of photogrammetric analyses of the landing site [*Kirk et al.*, this issue] will help refine surface facet orientations for targets of interest (including Yogi rock). Through these improvements, continued analysis of the photometry of Martian surface materials has the potential to enhance our understanding of surface properties at the SMS and provide important information relevant to assisting preparations for upcoming Mars lander missions.

Acknowledgments. We thank all members of the Mars Pathfinder Mission operations and support teams for their efforts and dedication to the Pathfinder mission, and we congratulate them on its success. We thank D. Domingue (JHU/APL) for her Hapke scattering model and many helpful discussions on its usage, and K. Becker, T. Becker, and J. Torson (USGS) for assistance with image mosaicking and spectra extraction software. We also thank P. Helfenstein (Cornell) for useful advice on the design of some IMP photometric imaging sequences, T. Daley (Cornell) for assistance with data reduction and analysis software, and valuable reviews from W. Calvin, H. Kieffer (USGS), and two anonymous reviewers.

References

Adams, J.B., M.O. Smith, and P.E. Johnson, Spectral mixture modeling: A new analysis of rock and soil types at the Viking Lander 1 site, *J Geophys. Res.*, *91*, 8098-8112, 1986.

Arnold, G., A. Dummerl, P. Lampen, F. Trauthan, P. Smith, D. Britt, J.R. Johnson, Laboratory spectrophotometric measurements of Mars analog materials and implications for the data evaluation of the Imager for Mars Pathfinder (IMP) (abstract), Europ. Geophy. Soc. Gen. Assemb. XXIII, *Ann. Geophys.*, *16*, C-1045, 1998.

Arvidson, R.E., E.A. Guinness, M.A. Dale-Bannister, J. Adams, M. Smith, P.R. Christensen, and R.B. Singer, Nature and distribution of surficial deposits in Chryse Planitia and vicinity, Mars, *J Geophys. Res.*, *94*, 1573-1587, 1989a.

Arvidson, R.E., J L. Gooding, and H.J. Moore, The Martian surface as imaged, sampled, and analyzed by the Viking landers, *Rev. Geophys*, *27*, 39-60, 1989b.

Banin, A., Clark, B.C., and H. Wanke, Surface chemistry and mineralogy, in *Mars*, edited by H.H. Kieffer, B.M. Jakosky, C.W. Snyder, and M.S. Matthews, Chap. 18, Univ. of Ariz. Press, Tucson, 1992.

Barron, V., and J. Torrent, Use of the Kubelka-Munk theory to study the influence of iron oxides on soil colour, *J. Soil Sci*, *37*, 499-510, 1986

Bell, J.F., III, and D. Crisp, Groundbased imaging spectroscopy of Mars in the near-infrared: Preliminary results, *Icarus*, *104*, 2-19, 1993.

Bell, J.F., III, T.B. McCord, and P.D. Owensby, Observational evidence of crystalline iron oxides on Mars, *J. Geophys. Res.*, *95*, 14,447-14,461, 1990.

Bell, J.F., III, R.V. Morris, and J.B. Adams, Thermally altered palagonitic tephra: A spectral and process analog to the soil and dust of Mars, *J Geophys. Res.*, 98, 3373-3385, 1993.

Bell, J.F., III, M.J. Wolff, T.C. Daley, D. Crisp, P.B. James, S.W. Lee, J.T. Trauger, and R.W. Evans, Near-infrared imaging of Mars from HST: Surface reflectance, photometric properties, and implications for MOLA data, in press, *Icarus*, 1999.

Binder A.B. and Jones J.C., Spectrophotometric studies of the photometric function, composition, and distribution of the surface materials of Mars, *J. Geophys. Res.*, *77*, 3005-3020, 1972.

Bishop, J.L, C.M. Pieters, R.G. Burns, J.O. Edwards, R.L. Mancinelli, and H. Froschl, Reflectance spectroscopy of ferric sulfate-bearing montmorillonites as Mars soil analog materials, *Icarus*, *117*, 101-119, 1995.

Blewett, D. T., P. G. Lucey, B.R. Hawke, G.G. Ling, and M.S. Robinson, A comparison of Mercurian reflectance and spectral quantities with those of the Moon, *Icarus*, *129*, 217-231, 1997.

Buratti, B.J., J.K. Hillier, and M. Wang, The lunar opposition surge: Observations by Clementine, *Icarus*, *124*, 490-499, 1996.

Clancy, R.T., and S.W. Lee, A new look at dust and clouds in the Mars atmosphere: Analysis of emission-phase-function sequences from global Viking IRTM observations, *Icarus*, *93*, 135-158, 1991.

Clancy, R.T., S.W. Lee, G R. Gladstone, W.W. McMillan, and T. Roush, A new model for Mars atmospheric dust based upon analysis of ultraviolet through infrared observations from Mariner 9, Viking, and Phobos, *J Geophys Res.*, *100*, 5251-5263, 1995.

Clark, B.E, et al., NEAR photometry of C-type asteroid 253 Mathilde (abstract 1768), *Lunar Planet Sci. Conf, XXIX* [CD-ROM], 1998.

Clark, I.H D., A three-dimensional tilted-facet surface reflectance and volume scattering model for coated rock surfaces (abstract 1846), *Lunar Planet. Sci. Conf, XXIX*, [CD-ROM], 1998.

de Grenier, M., and P.C. Pinet, Near-opposition Martian limb darkening: Quantification and implication for visible-near-infrared bidirectional reflectance studies, *Icarus*, *115*, 354-368, 1995.

Domingue, D., and B. Hapke, Disk-resolved photometric analysis of Europan terrains, *Icarus*, *99*, 70-81, 1992.

Domingue, D., G.W. Lockwood, and D.T. Thompson, Surface textural properties of icy satellites: A comparison between Europa and Rhea, *Icarus*, *115*, 228-249, 1995.

Domingue, D., B. Hartman, and A. Verbiscer, The scattering properties of natural terrestrial snows versus icy satellite surfaces, *Icarus*, *128*, 28-48, 1997.

Eliason, E.M., Production of digital image models using the ISIS system (abstract), *Lunar Planet. Sci. Conf, XVIII*, 331-332, 1997.

Erard, S., A spectrophotometric model of Mars in the near-infrared, (abstract 1214), *Lunar Planet Sci. Conf., XXIX*, [CD-ROM], 1998.

Gaddis, L, et al., An overview of the Integrated Software for Imaging Spectrometers (ISIS) (abstract), *Lunar Planet. Sci. Conf., XVIII*, 387-388, 1997.

Gaddis, L R., et al., Digital mapping of the Mars pathfinder landing site: design, acquisition, and derivation of cartographic products for science applications, *J Geophys. Res.*, this issue.

Golombek, M.P., et al., Overview of the Mars Pathfinder mission and assessment of landing site predictions, *Science*, *278*, 1743-1748, 1997.

Gooding, J.L., R.E. Arvidson, and M.Y. Zolotov, Physical and chemical weathering, in *Mars*, edited by H.H. Kieffer, B.M. Jakosky, C.W. Snyder, and M.S. Matthews, Chap. 19, Univ. of Ariz. Press, Tucson, 1992.

Guinness, E.A., Spectral properties (0.40 to 0.75 microns) of soils exposed at the Viking 1 landing site, *J Geophys. Res.*, *86*, 7983-7992, 1981.

Guinness, E.A., R.E. Arvidson, D.C. Gehret, and L.K. Bolef, Color changes at the Viking landing sites over the course of a Mars year, *J. Geophys Res.*, *84*, 8355-8364, 1979.

Guinness, E.A , R.E. Arvidson, M.A. Dale-Bannister, R.B. Singer, and E.A. Bruckenthal, On the spectral reflectance properties of materials exposed at the Viking landing sites, *Proc. Lunar Planet. Sci. Conf. 7th*, Part 2, *J. Geophys Res.*, *92*, suppl., E575-E587, 1987.

Guinness, E.A., R.E. Arvidson, and M.K. Shepard, Specular scattering from rock surfaces at the Viking lander sites (abstract), *Lunar Planet. Sci Conf., XXVII*, 471-472, 1996.

Guinness, E.A., R.E. Arvidson, M.K. Shepard, and I. Clark, Optical scattering properties of terrestrial varnished basalts compared with rocks and soils at the Viking lander sites (abstract), *Lunar Planet. Sci Conf., XXVIII*, 491-492, 1997a.

Guinness, E.A., R.E. Arvidson, I.H.D. Clark, and M.K. Shepard, Optical scattering properites of terrestrial varnished basalts compared with rocks and soils at the Viking Lander sites, *J Geophys. Res*, *102*, 28,687-28,703, 1997b.

Hapke, B., The photometric function of Martian soil in the vicinity of Viking lander 1, in *Reports on the Planetary Geology Program 1978-1979, NASA Tech. Memo*, *80339*, 410, 1979.

Hapke, B., Bidirectional reflectance spectroscopy, 3, Correction for macroscopic roughness, *Icarus*, *59*, 41-59, 1984.

Hapke, B., Bidirectional reflectance spectroscopy, 4, The extinction coefficient and the opposition effect, *Icarus*, *67*, 264-280, 1986.

Hapke, B., *Theory of Reflectance and Emittance Spectroscopy*, 455 pp., Cambridge Univ. Press, New York, 1993.

Hapke, B., R. Nelson, and W. Smythe, The opposition effect of the Moon: Coherent backscatter and shadow hiding, *Icarus*, 133, 89-97, 1998.

Hartman, B., and D. Domingue, Scattering of light by individual particles and the implications for models of planetary surfaces, *Icarus*, *131*, 421-448, 1998.

Helfenstein, P. and J. Veverka, Photometric properties of lunar terrains derived from Hapke's equation, *Icarus*, *72*, 342-357, 1987.

Helfenstein, P., et al., Galileo photometry of asteroid 243 Ida, *Icarus*, *120*, 48-65, 1996.

Helfenstein, P., J. Veverka, and J. Hillier, The lunar opposition effect: A test of alternative models, *Icarus*, *128*, 2-14, 1997.

Hillier, J.K., Shadow-hiding opposition surge for a two-layer surface, *Icarus*, *128*, 15-27, 1997a.

Hillier, J.K., Scattering of light by composite particles in a planetary surface, *Icarus*, *130*, 328-335, 1997b.

Huck, F.O., D.J. Jobson, S.K. Park, S.D. Wall, R.E. Arvidson, W.Patterson, and W.Benton, Spectrophotometric and color estimates of the Viking lander sites, *J. Geophys. Res.*, *82*, 4401-4411, 1977.

Hviid, S.F., et al., Magnetic properties experiments on the Mars Pathfinder lander: Preliminary results, *Science*, *278*, 1768-1770, 1997.

Israel, E.J., R.E. Arvidson, A. Wang, J.D. Pasteris, and B.L. Jolliff, Laser Raman spectroscopy of varnished basalt and implications for in situ measurements of Martian rocks, *J Geophys. Res.*, *102*, 28,705-28,716, 1997.

Kirk, R.L., E. Howington-Kraus, T. Hare, E. Dorrer, D. Cook, M. Gordon, K. Becker, B. Redding, J. Blue, and E.M. Lee, Digital photogrammetric analysis of the IMP camera images: Mapping the Mars Pathfinder landing site in three dimensions, *J Geophys Res.*, this issue.

Kirkland, L., A. Treiman, and S. Murchie, Photometry of bright regions on Mars: ISM results (abstract), *Lunar Planet. Sci. Conf., XXVIII*, 729-730, 1997.

Liang, S., and J.R.G. Townshend, A modified Hapke model for soil bidirectional reflectance, *Remote Sens. Environ* , *55*, 1-10, 1996.

McEwen, A.S., Photometric functions for photoclinometry and other applications, *Icarus*, *92*, 298-311, 1991.

McEwen, A.S.,A precise lunar photometric function (abstract), *Lunar Planet. Sci. Conf., XXVII*, 841-842, 1996.

McGuire, A.F., and B.W. Hapke, An experimental study of light scattering by large, irregular particles, *Icarus*, *113*, 134-155, 1995.

McSween, H.Y., Jr., et al., Chemical, multispectral, and textural constraints on the composition and origin of rocks at the Mars Pathfinder landing site, *J. Geophys. Res.*, this issue.

Minnaert, M., The reciprocity principle in lunar photometry, *Astrophys. J. 93*, 403-410, 1941.

Mustard, J.F., and C.M. Pieters, Photometric phase functions of common geologic minerals and applications to quantitative analysis of mineral mixture reflectance spectra, *J. Geophys. Res.*, *94*, 13,619-13,634, 1989.

Nelson, R.M., B.W. Hapke, W.D. Smythe, and L.J. Horn, Phase curves of selected particulate materials: The contribution of coherent backscattering to the opposition surge, *Icarus*, *131*, 223-230, 1998.

Pollack, J.B., D. Colburn, F.M. Flasar, R. Kahn, C. Carlston, and D. Pidek, Properties and effects of dust particles suspended in the Martian atmosphere, *J. Geophys Res.*, *84*, 2929-2945, 1979.

Pollack, J.B., M.E. Ockert-Bell, and M.K. Shepard, Viking lander image analysis of Martian atmospheric dust, *J Geophys. Res.*, *100*, 5235-5250, 1995.

Privette, J.L., R.B. Myneni, W.J. Emery, and B. Pinty, Inversion of a soil bidirectional reflectance model for use with vegetation reflectance models, *J. Geophys Res.*, *100*, 25,497-25,508, 1995.

Reid, R.J., et al., IMP image calibration, *J. Geophys. Res* , this issue.

Rieder, R., T. Economou, H. Wanke, A. Turkevich, J. Crisp, J. Bruckner, G. Dreibus, and H.Y. McSween Jr, The chemical composition of martian soil and rocks returned by the mobile alpha proton X-ray spectrometer: Perliminary results from the X-ray mode, *Science*, *278*, 1771-1774, 1997.

Roush, T.L., D.L. Blaney, and R.B. Singer, The surface composition of Mars as inferred from spectroscopic observations, in *Remote Geochemical Analysis. Elemental and Mineralogical Composition*, pp. 367-393, Cambridge Univ. Press, New York, 1993.

Rover Team, Characterization of the martian surface deposits by the Mars Pathfinder rover, Sojourner, *Science*, *278*, 1765-1768, 1997.

Schultz, P.H., and J.F. Mustard, Martian impact glass: Generation and evidence (abstract 1847), *Lunar Planet Sci. Conf., XXIX*, [CD-ROM], 1998.

Simonelli, D.P., M. Wisz, A. Switala, D. Arnolfi, J. veverka, P.C. Thomas, and P Helfenstein, Photometeric properties of Phobos surface materials from Viking images, *Icarus*, *131*, 52-77, 1998.

Singer, R.B., and H.Y. McSween, Jr., The igneous crust of Mars: Compositional evidence from remote sensing and the SNC meteorites, in *Resources of Near-Earth Space*, pp. 709-736, Univ. of Ariz. Press, Tucson, 1993.

Singer, R.B., T. B. McCord, R. N. Clark, J.B. Adams, and R.L. Huguenin, Mars surface composition from reflectance spectroscopy: A summary, *J. Geophys. Res.*, *84*, 8415-8426, 1979.

Smith, P.H., et al., The imager for Mars Pathfinder experiment, *J. Geophys. Res.*, *102*, 4003-4026, 1997a.

Smith, P.H., et al., *Science*, *278*, 1758-1765, 1997b.

Smith, P.H., and M.T. Lemmon, Opacity of the Martian atmosphere measured by the Imager for Mars Pathfinder, *J. Geophys. Res.*, this issue.

Soderblom, L.A., The composition and mineralogy of the martian surface from spectroscopic observations: 0.3 μm to 50 μm, in *Mars*, edited by H.H. Kieffer, B.M. Jakosky, C.W. Snyder, and M.S. Matthews, Chap. 17, Univ. of Ariz. Press, Tucson, 1992.

Thomas, P.C., D. Adinolfi, P. Helfenstein, D. Simonelli, and J. Veverka, The surface of Deimos: Contribution of materials and processes to its unique appearance, *Icarus*, *123*, 536-556, 1996.

Thomas, N., W.J. Markiewicz, R.M. Sablotny, M.W. Wuttke, H U. Keller, J.R. Johnson, R.J. Reid, and P.H. Smith, The color of the Martian sky and its influence on the illumination of the Martian surface, *J Geophys Res.*, this issue.

Thorpe T.E., Viking Orbiter photometric observations of the Mars phase function: July through November 1976, *J. Geophys. Res.*, *82*, 4161-4165, 1977.

Tomasko, M.G., L.R. Doose, M.T. Lemmon, P.H. Smith, and E. Wegryn, Properties of dust in the Martian atmosphere from the imager on Mars Pathfinder, *J Geophys. Res.*, this issue.

Veverka, J., P. Helfenstein, B. Hapke, and J.D. Goguen, Photometry and polarimetry of Mercury, in *Mercury*, edited by C. Chapman, pp. 37-58, Univ. of Ariz. Press, Tucson, 1988.

Young, A.T., and S.A. Collins, Photometric properties of the Mariner cameras and of selected regions on Mars, *J. Geophys Res.*, *76*, 432-437, 1971.

R. Anderson, N. T. Bridges, and J. Maki, Jet Propulsion Laboratory, Pasadena, CA 91103.

G. Arnold, A. Dummel, R. Jaumann, and F. Trauthan, DLR, Institute of Planetary Exploration, Rudower Chaussee 5, 12489, Berlin, Germany.

J. F. Bell III, Center for Radiophysics and Space Research, 424 Space Sciences Building, Cornell University, Ithaca, NY 14853-6801.

D. T. Britt, M Lemmon, R. J. Reid, and P. Smith, Lunar and Planetary Laboratory, University of Arizona, Tucson, AZ 85721.

L. Gaddis, K. E. Herkenhoff, J. R. Johnson, R Kirk, and L. A. Soderblom, 2255 North Gemini Drive, Branch of Astrogeology, U.S. Geological Survey, Flagstaff, AZ 86001. (e-mail: jjohnson@flagmail.wr.usgs.gov).

S. Murchie, Applied Physics Laboratory, Johns Hopkins University, Johns Hopkins Road, Laurel, MD 20723.

N. Thomas, Max Planck Institute for Aeronomy, Postfach 20, Katlenburg-Lindau, D-3411, Germany.

(Received February 23, 1998; revised June 5, 1998;
accepted June 30, 1998.)